Published April 29, 2013

Release of cellular tension signals self-restorative ventral lamellipodia to heal barrier micro-wounds

Roberta Martinelli,[1] Masataka Kamei,[1] Peter T. Sage,[1] Ramiro Massol,[3] Laya Varghese,[1] Tracey Sciuto,[2] Mourad Toporsian,[1] Ann M. Dvorak,[2] Tomas Kirchhausen,[3,4,5] Timothy A. Springer,[3,4,6] and Christopher V. Carman[1]

[1]Department of Medicine and [2]Department of Pathology, Center for Vascular Biology Research, Beth Israel Deaconess Medical Center, Harvard Medical School, Boston, MA 02215
[3]Department of Pediatrics and [4]The Immune Disease Institute, Children's Hospital, Harvard Medical School, Boston, MA 02115
[5]Department of Cell Biology and [6]Department of Biological Chemistry and Molecular Pharmacology, Harvard Medical School, Boston, MA 02115

Basic mechanisms by which cellular barriers sense and respond to integrity disruptions remain poorly understood. Despite its tenuous structure and constitutive exposure to disruptive strains, the vascular endothelium exhibits robust barrier function. We show that in response to micrometer-scale disruptions induced by transmigrating leukocytes, endothelial cells generate unique ventral lamellipodia that propagate via integrins toward and across these "micro-wounds" to close them. This novel actin remodeling activity progressively healed multiple micro-wounds in succession and changed direction during this process. Mechanical probe-induced micro-wounding of both endothelia and epithelia suggests that ventral lamellipodia formed as a response to force imbalance and specifically loss of isometric tension. Ventral lamellipodia were enriched in the Rac1 effectors cortactin, IQGAP, and p47Phox and exhibited localized production of hydrogen peroxide. Together with Apr2/3, these were functionally required for effective micro-wound healing. We propose that barrier disruptions are detected as local release of isometric tension/force unloading, which is directly coupled to reactive oxygen species–dependent self-restorative actin remodeling dynamics.

Introduction

Maintenance of tissue barriers requires the ability to cope with diverse biomechanical strains. The vascular endothelium serves as the critical partition between the blood circulation and the interstitium, and failure of this barrier has devastating consequences (Aird, 2007). Endothelia function in the constitutive presence of extreme biomechanical stresses such as variable fluid shear, stretch, and hydrostatic pressure. Yet most of the body's ~5,000 m^2 of endothelium (Hwa et al., 2005) is a simple and thin (<1 µm; Feng et al., 2002) monolayer of endothelial cells attached to a basement membrane via integrin receptors and held to each other by intercellular adherens, tight, and gap junctions (Bazzoni and Dejana, 2004). The fundamental cellular and molecular mechanisms that maintain integrity of this tenuous structure remain poorly understood.

Among the significant biomechanical challenges faced by the endothelium is the trafficking of blood and stem cells. There are many settings in which such cells must repeatedly cross the vasculature to enter and leave the circulation, a process termed diapedesis or transendothelial migration (Sage and Carman, 2009). This requires localized breakage of cell–cell and cell–matrix adhesions in the endothelium and the formation of micron-scale transcellular pores and paracellular gaps that accommodate diapedesis. Such discontinuities serve as physiological passageways, yet also represent a liability to vascular integrity and hence could be regarded as "micro-wounds." Diapedesis micro-wounds form largely as a result of mechanical forces exerted by the trafficking cells through F-actin protrusions such as pseudopodia and invasive podosomes (Ley et al., 2007; Carman, 2009a,b).

In vitro transmigration pores and gaps disappear rapidly after diapedesis (Shaw et al., 2001; Carman and Springer, 2004;

R. Martinelli and M. Kamei contributed equally to this paper.

Correspondence to Christopher V. Carman: ccarman@bidmc.harvard.edu

Abbreviations used in this paper: DIC, differential interference contrast; DPI, diphenylene iodonium; IRM, interference-contrast reflection microscopy; MVEC, microvascular endothelial cell; ROS, reactive oxygen species; TIRF, total internal reflection fluorescence; VL, ventral lamellipodia; VW, ventral F-actin wave.

Supplemental Material can be found at:
http://jcb.rupress.org/content/suppl/2013/04/24/jcb.201209077.DC1.html
Original image data can be found at:
http://jcb-dataviewer.rupress.org/jcb/browse/6308

The Rockefeller University Press $30.00
J. Cell Biol. Vol. 201 No. 3 449–465
www.jcb.org/cgi/doi/10.1083/jcb.201209077

Published April 29, 2013

Cinamon et al., 2004; Yang et al., 2005; Millán et al., 2006). In vivo, remarkably little leakage of blood plasma (or macromolecular tracers) into tissues is evident at sites of leukocyte transendothelial migration (Thureson-Klein et al., 1986; Gawlowski et al., 1993; Sage and Carman, 2009; Kim et al., 2009; He, 2010). Moreover, even under conditions of frequent leukocyte trafficking, open (i.e., leukocyte-free) pores or gaps are rarely seen (Marchesi and Florey, 1960; De Bruyn et al., 1971; Campbell, 1972; Chamberlain and Lichtman, 1978; Cho and De Bruyn, 1986; Feng et al., 1998; Hoshi and Ushiki, 1999; Woodfin et al., 2011). Finally, leukocyte-independent mechanical stresses can also produce appreciable steady-state endothelial microwounding in vivo, but without significant vascular breakdown (McNeil and Ito, 1990; Yu and McNeil, 1992). Thus, existence of proactive mechanisms that efficiently reestablish integrity are strongly implied. In this study we address the critical question of how micro-wounds are "healed" after diapedesis or direct mechanical micro-disruption. We uncover a novel Rac1- and reactive oxygen species (ROS)–dependent actin remodeling activity—directed ventral lamellipodia (VL)—that serve this function. This, together with additional biomechanical manipulations in endothelia and epithelia, lead us to propose a general tension-based model for integrity sensing whereby localized tension loss during adhesion rupture positively signals its own repair.

Results

Leukocyte-driven endothelial micro-wounds are closed efficiently

To investigate endothelial remodeling during diapedesis, we used in vitro models of inflammatory leukocyte recruitment. Monolayers of human dermal or lung microvascular endothelial cells (MVECs) were transfected with a fluorescent membrane marker (i.e., mYFP, mDsRed, or ICAM-1-GFP) and activated with TNF. Coincubated lymphocytes avidly adhered to, spread on, and transmigrated across these monolayers through formation of ∼3–6-µm transcellular pores and paracellular gaps (Fig.1 a, yellow lines). When imaged over time, we confirmed that pores and gaps rapidly closed (Fig.1 a, red lines) after completion of diapedesis events and that endothelial cells possessed a robust capacity to restore numerous discontinuities concomitantly and successively.

Transcellular pore closure is initiated by newly described VL

We hypothesized that the closure of transcellular pores might involve a "purse string" mechanism, whereby F-actin would accumulate symmetrically around the pore and contract. Strikingly, we found that transcellular pore closure proceeded through a largely asymmetric process. Dynamic bursts of actin formed on one side of the pore and then rapidly moved across it (Fig.1 b and Video 1, Part I, A). These were initiated just before or after the final exit of the lymphocyte from the pore and then propagated for a mean of 16.38 ± 1.2 µm (width of 12.71 ± 1.07 µm, velocities of 2.91 ± 0.18 µm/min) with lifetimes of 6.38 ± 0.5 min before being extinguished (Fig. 1 c).

For a minority (∼20%) of events the actin bursts were initiated precisely at the border of the pore and traveled just to the opposite edge where they disappeared along with the micro-wound (Fig. S1 a and Video 2, Part I, type A). In the majority of cases (∼80%) these actin structures exhibited propagation outside the confines of the pore. That is, they initiated at sites adjacent to the micro-wound (∼0.5–15 µm away; mean of 4.61 ± 0.49 µm) and/or moved beyond its distal edge after closing it (∼0.5–30 µm; mean of 8.17 ± 0.99 µm; Fig. 1 d; Fig. S1, b and c; and Video 2, Part I, type B and C). At high lymphocyte/diapedesis density single bursts processively traveled through and closed multiple endothelial pores (Fig. S1 c and Video 2, Part I, type C). During propagation outside of the pore the mDsRed intensity doubled, suggesting membrane folding (Fig. 1 e and Video 1, Part II). Similar results were found using a range of molecularly distinct membrane markers (e.g., farnesylated GFP, GPI-GFP, and R18; unpublished data). This implies that the actin bursts are contained in membrane surface protrusions (i.e., lamellipodia- or ruffle-like structures).

We next asked on which surface (i.e., dorsal/apical or ventral/basal) these protrusions formed. Total internal reflection fluorescence (TIRF) microscopy (using mYFP; Fig. 2 a) and interference-contrast reflection microscopy (IRM; not depicted), complementary modalities for detecting close (<100 nm) cell–substrate apposition, showed that the pore-closing protrusions (without exception in 24 measurements) formed underneath the endothelium. Further confirmation of this was obtained using spinning-disk confocal imaging (Fig. 2 b and Video 3). Ultrastructural electron microscopy views of basal F-actin–rich VL were also detected (Fig. 2, c and d).

We considered that the unique ventral orientation of these protrusions was due in part to roles for integrin–substrate interaction. Both α5 and β3 integrins showed enrichment in VL compared with adjacent regions (Fig. 2 e, i and ii). Addition of function-blocking antibodies against both α5β1 and αVβ3 caused VL to lift off the substrate and retract (Fig. 2 e, iii and iv, red arrowheads) and failed pore closure (Fig. 2 e, iii–v). Whereas 97.3% of pores closed within 10 min in control settings, only 7.1% closed in the presence of blocking antibody. Thus, endothelial VL require integrin–matrix adhesion to effectively propagate.

Endothelia form distinct "ventral waves" that coexist with VL

Our characterization of VL up to this point indicated some resemblance to ventral F-actin waves (VW) observed in motile *Dictyostelium discoideum*, fibroblasts, neutrophils, and tumor cells (Vicker, 2002; Weiner et al., 2007; Case and Waterman, 2011). As with VL, VW exhibit integrin-mediated basal propagation. However, VW do not form membrane protrusions until they reach a cell border (indicated by an absence of membrane folding/doubling [Bretschneider et al., 2004]) and travel as clusters of actin punctae rather than a continuous leading edge. Via combined fluorescence and IRM imaging we found that resting endothelial cells spontaneously formed VW, but not VL (Fig. S2 a). The VW traveled in all directions (at 1.1 ± 0.96 µm/min) and exhibited frequent turning (36%), bifurcation (68%), and

Published April 29, 2013

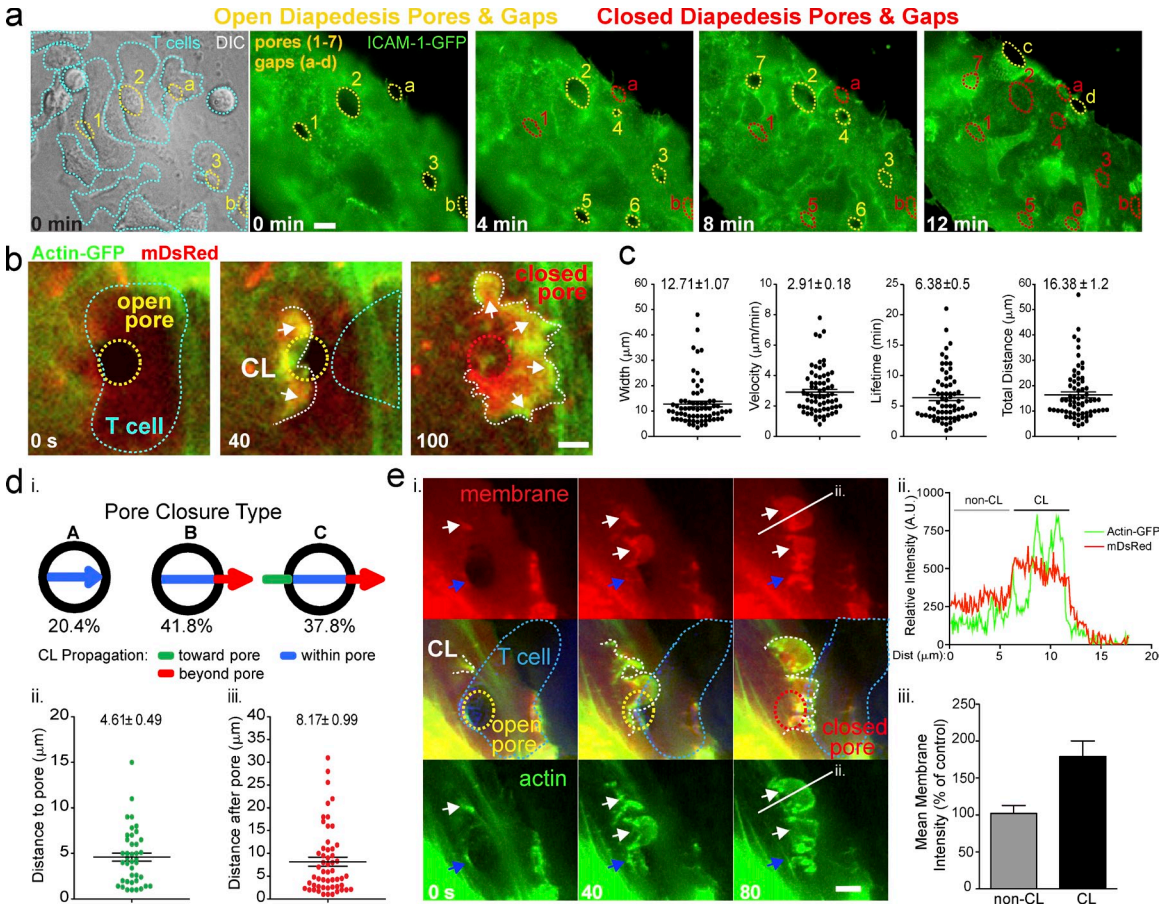

Figure 1. **Transcellular endothelial micro-wounds are closed efficiently after diapedesis through bursts of lamellar activity.** Live-cell imaging of lymphocyte diapedesis through MVECs. (a) DIC and fluorescence imaging of migrating T cells (cyan outlines) on an ICAM-1-GFP–expressing endothelial cell (green). Open diapedesis pores (1–3) and gaps (a and b) associated with T cells in the process of diapedesis are outlined in yellow. The subsequent time points show opening of additional pores (4–7) and gaps (c and d) formed by other T cells initiating diapedesis. The progressive closure of the pores and gaps after completion of each diapedesis event is denoted by a switch from yellow to red outlines. (b) Representative time series of a pore closure event in MVECs coexpressing actin-GFP and mDsRed. Yellow outline shows an open transcellular pore associated with a T cell (cyan outline) that has nearly completed diapedesis. A pore closing structure (CL; white arrows and dashed line) is evident as a burst of actin and membrane traveling across the pore to close it. See Video 1, Part I. (c) Analysis of width and dynamics of >68 individual pore closing structures. (d) Percentage of three classes (Fig. S1 a) of pore closing types (i) and quantitative analysis of CL travel distances (ii and iii). $n > 100$. (e) Doubling/Folding of membrane during pore closure. (i). Arrows indicate actin protrusions initiated at the edge of the pore (blue) and at distant sites (white). White line shows location of a fluorescence intensity line scan analysis (ii) with regions that are part of (CL) and outside of (non-CL) the closure structure indicated. (iii) Membrane fluorescence analysis in CL and non-CL structures. $n = 15$. Error bars represent SEM. See Video 1, Part II. Bars, 5 μm.

self-annihilation upon intersection (Fig. S2, b, c, and e). What regulates, and the functional roles for, these wound-independent VW remain unknown.

During diapedesis, VW and VL could be seen to coexist both independently at distinct locations and coordinately at sites of wound closure (Fig. S2 d). A subset of VL (~20%) was followed by VW-type actin punctae that traveled ~2–3 μm behind the leading edge and continued to propagate after VL extinction (Fig. S2 d and Video 4, Part I, ex. 3). Thus, although VL and VW can each form independently in endothelium, these two modes of actin propagation can coexist and possibly interchange during pore closure events.

VL initiate closure of paracellular diapedesis gaps

We next focused on the closure of paracellular diapedesis gaps. Here we found again a process involving local bursts of lamellipodial activity (Fig. 3 a and Video 1 B). These structures (width of 12.9 ± 1 μm) traveled peripherally (at 2.8 ± 0.2 μm/min; lifetime of 6.3 ± 0.6 min) to fill the gaps and reestablish overlapping contacts with the neighboring endothelial cells (Fig. 3, a and b). Whereas in ~63% of events the lamellipodia were initiated at the endothelial cell edge, ~37% of them were initiated ≥1 μm away (with doubled mDsRed intensity; Fig. 3, a [i] and c).

Live imaging of VL-driven gap closure showed rapid assembly of VE-cadherin-GFP punctae into linear arrays to reestablish the adherens junctions (Fig. 3 d). Live-cell imaging followed by fixation, staining, and reimaging of the same field showed that within ~5 min of gap closure, adherens junctions with strongly co-localized endogenous VE-cadherin and β-catenin were reconstituted and indistinguishable from adjacent unperturbed junctional segments (Fig. 3 e, iii).

Thus, despite clear distinctions in transcellular pores and paracellular gaps, endothelial cells use similar VL mechanisms for their closure. The same was true for diapedesis of granulocytes (Fig. S1 d and Video 2, Part II, ex.1) and monocytes (not depicted)

Published April 29, 2013

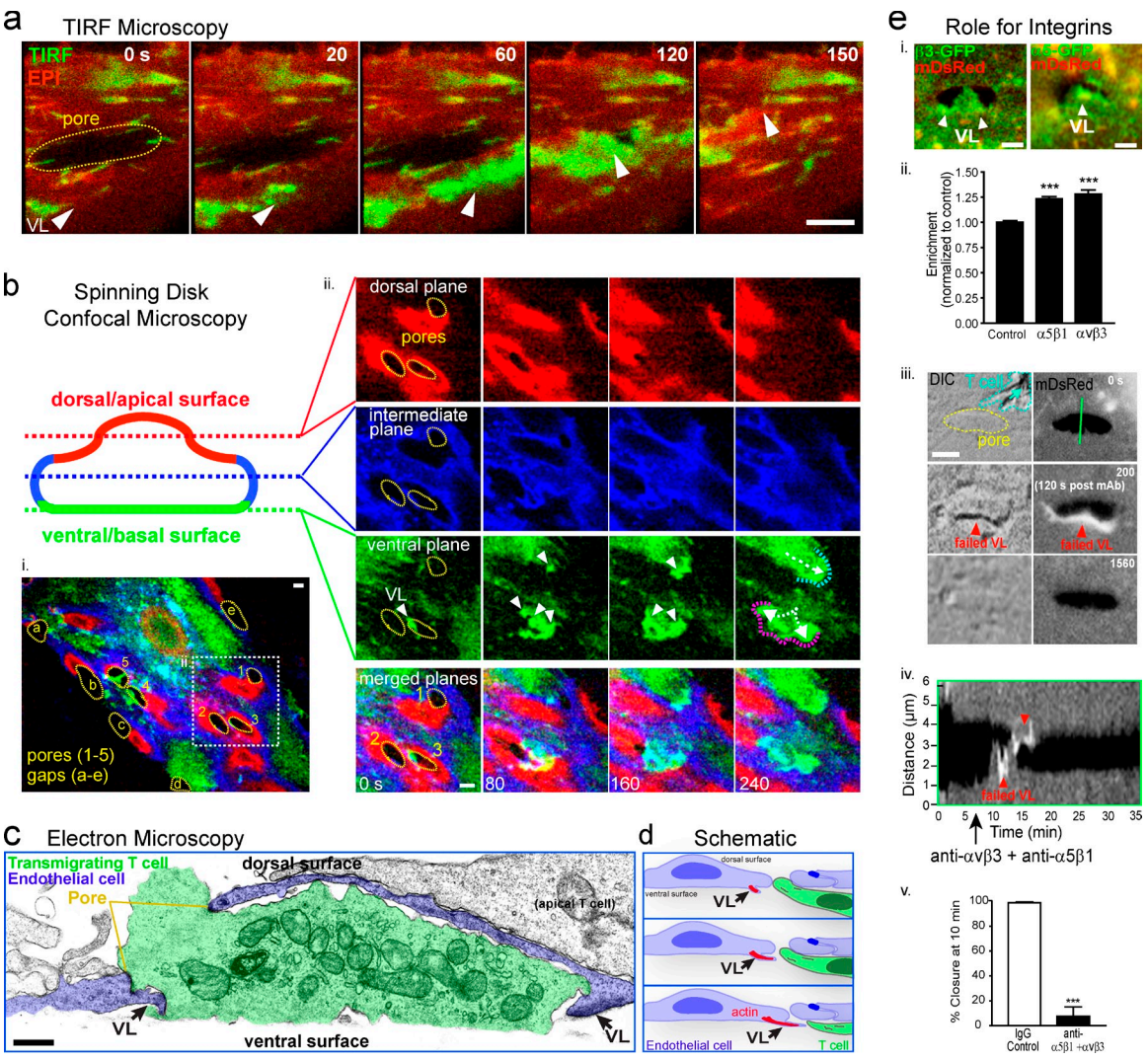

Figure 2. **Transcellular pore closure is initiated by novel VL.** (a) Combined epifluorescence (red) and TIRF (green) imaging of diapedesis pore (yellow line) being closed by a lamellar structure in an MVEC expressing mDsRed. Arrowheads show a high TIRF signal indicating a VL. (b, i) Dynamic serial-section spinning disk confocal imaging of a mYFP-expressing endothelial cell during T cell diapedesis. Sections of dorsal/apical (red), intermediate (blue), and ventral/basal (green) planes were differentially pseudo-colored and overlaid. Dashed yellow lines indicate transcellular pores (1–5) and paracellular gaps (a–e) where individual T cells are transmigrating. (ii) Expanded view of the boxed region in panel i shows membrane protrusions (VL, arrowheads) formed in the ventral plane spreading under three pores. See Video 3. (c) Ultrastructural view of basal F-actin–rich protrusions putatively representing VL (arrows) during late stages of T cell (green) diapedesis across the endothelium (blue). (d) Schematic model of VL pore closure. (e) Representative images (i) and membrane-normalized quantitation (ii) of β3-GFP and α5-GFP integrin distribution within pore-closing VL. (iii–v) Anti-αvβ3 and -α5β1 function-blocking antibodies were added immediately after exit of a T cell (cyan outline) from a diapedesis pore. (iii) Representative images show VL that initially protrude and then retract. Green line (iii) traces location used for kymograph representation (iv). (v) Percentage of pores that closed in the 10 min after addition of blocking antibodies. Values represent mean ± SEM; $n > 20$. Bars, 5 μm.

on a range of endothelial cell types (i.e., human umbilical vein endothelial cell and human cardiac MVEC; not depicted) and under physiological fluid shear flow (Fig. S1 e and Video 2, Part II, ex. 2). Moreover, similar pore-closing VL also formed after transcellular diapedesis of lymphocytes across CHO-K1 epithelial cells, demonstrating that VL-mediated micro-wound healing is not endothelial restricted (Fig. S1 f and Video 2, Part II, ex. 3).

VL are preferentially nucleated from preexisting actin filaments

To gain insights into VL regulatory mechanisms, we analyzed their initiation dynamics. We found, in >400 observations, that VL only formed in response to micro-wounding and that the majority emerged from preexisting actin filaments within ∼5 μm of a pore or gap. Such "parent filaments" were of varied radial and tangential orientations with respect to the micro-wound and had all undergone discernible retraction, breakage, or distortion during the diapedesis event (Fig. 4). These filaments briefly (10–40 s) formed a discrete node of increased actin density, which then transitioned to small VL that were visible as either a small crescent on one side of the filament, a spade on both sides or at the end of a filament, or a fan between two of them (Fig. 4 a). In a subset of events, the node was evident as a discrete spike (∼300–600 nm in length). Quantitation showed that spikes projected at angles between 45° and 80°, but averaged ∼70° (69.1 ± 1.9; Fig. 4 b, iii), suggesting possible involvement

Published April 29, 2013

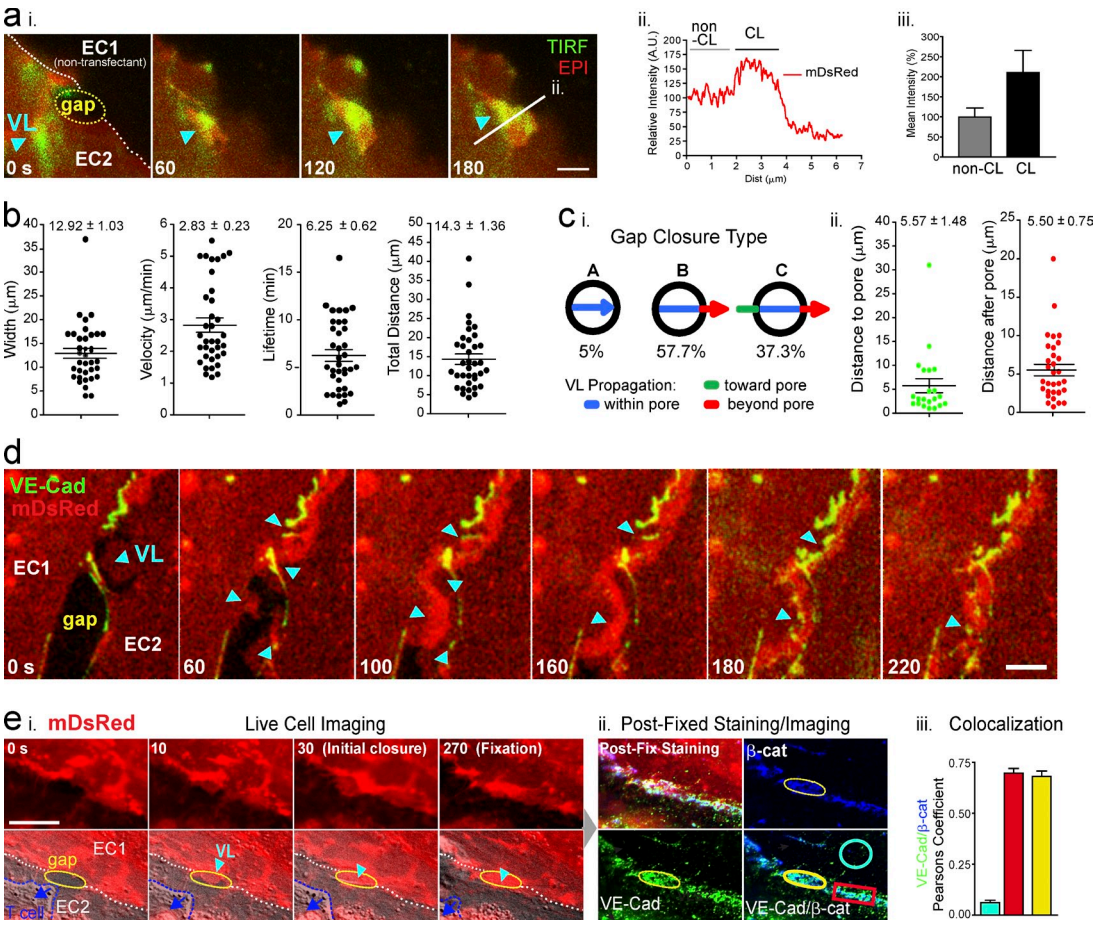

Figure 3. **VL initiate closure of paracellular diapedesis gaps.** (a) Dynamic epifluorescence (red) and TIRF (green) imaging of a paracellular diapedesis gap (yellow line) closure in an MVEC by a membrane protrusion (VL, arrowhead). Strong TIRF signal (i) and doubling of epifluorescence intensity (i–iii) demonstrate propagation as VL. $n > 30$. (b) Analysis of width and dynamics of VL. $n > 35$. (c) Percentage of three VL classes (i) and analysis of VL travel distances (ii). $n > 100$. (d) Dynamic imaging of mDsRed (red) and VE-cadherin-GFP (green) during gap closure. Cyan arrowheads indicate VL-mediated restoration of intercellular contacts followed by accumulation of VE-cadherin. (e) MVECs expressing mDsRed were imaged during gap closure (cyan arrowhead; i), fixed and stained for VE-cadherin and β-catenin (ii), and subjected to Pearson's colocalization analysis (iii). $n > 18$. Bars, 5 μm. All values are mean ± SEM.

of the Arp2/3 complex. In all cases, despite diverse initial orientations, the expanding VL always ultimately radiated toward the micro-wound (Video 4).

VL exhibit unique directed propagation and "steering" capacity

We next analyzed the directionality of VL propagation. When we assessed VL movement with respect to radial axes of symmetry of the endothelial cells (Fig. 5 a, i–iii) we found that during pore closure ∼60% of VL were initiated at a relatively central location with respect to the pore and therefore traveled peripherally to reach and close it (Fig. 5 a, ii). Alternatively, 13% of VL propagated centripetally and 27% moved orthogonally (laterally; Fig. 5 a, ii). During closure of gaps the majority of VL propagated peripherally, but ∼28% traveled along the axis of the adherens junctions (Fig. 5 a, iii). Furthermore, pores/gaps were often healed by two or more VL that moved in different directions toward the micro-wound (Fig. 5 b and Video 4, Part II, ex. 1). Thus, VL initiation locus and propagation direction are not prescribed by the axes of symmetry within the endothelial cell, as is the case for leading edge lamellipodia and dorsal ruffles (Chhabra and Higgs, 2007).

We compared directionality of VL propagation with that of the transmigrated lymphocyte. Although ∼38% of the VL moved parallel to the direction of the subendothelial lymphocyte, VL mostly traveled in a direction that was orthogonal or antiparallel to that of the T cell (Fig. 5 c). Aborted transmigration events, whereby the T cell reversed direction to the apical side after forming a pore or gap, were closed similarly (e.g., Video 1 B). Hence, VL propagation directionality is not coupled to the migration direction of the leukocyte that formed the micro-wound.

Our analysis also indicated a capacity of VL to adjust their direction. Initially, ∼20% of VL were poorly oriented toward their target micro-wound. These then steered toward the pore or gap, turning as much as 180° (Fig. 5 d). Individual VL processively healed multiple micro-wounds in succession and adjusted their course repeatedly during in this process (Fig. 5, e and f; and Video 4, Part II, ex. 2 and 3). Our collective analyses show that VL may be initiated from preexisting actin filaments within ∼5 μm of a pore/gap and then consistently steer toward them. This suggests a complex ability of the endothelium to sense local discontinuities and integrate subcellular-scale spatial information.

Published April 29, 2013

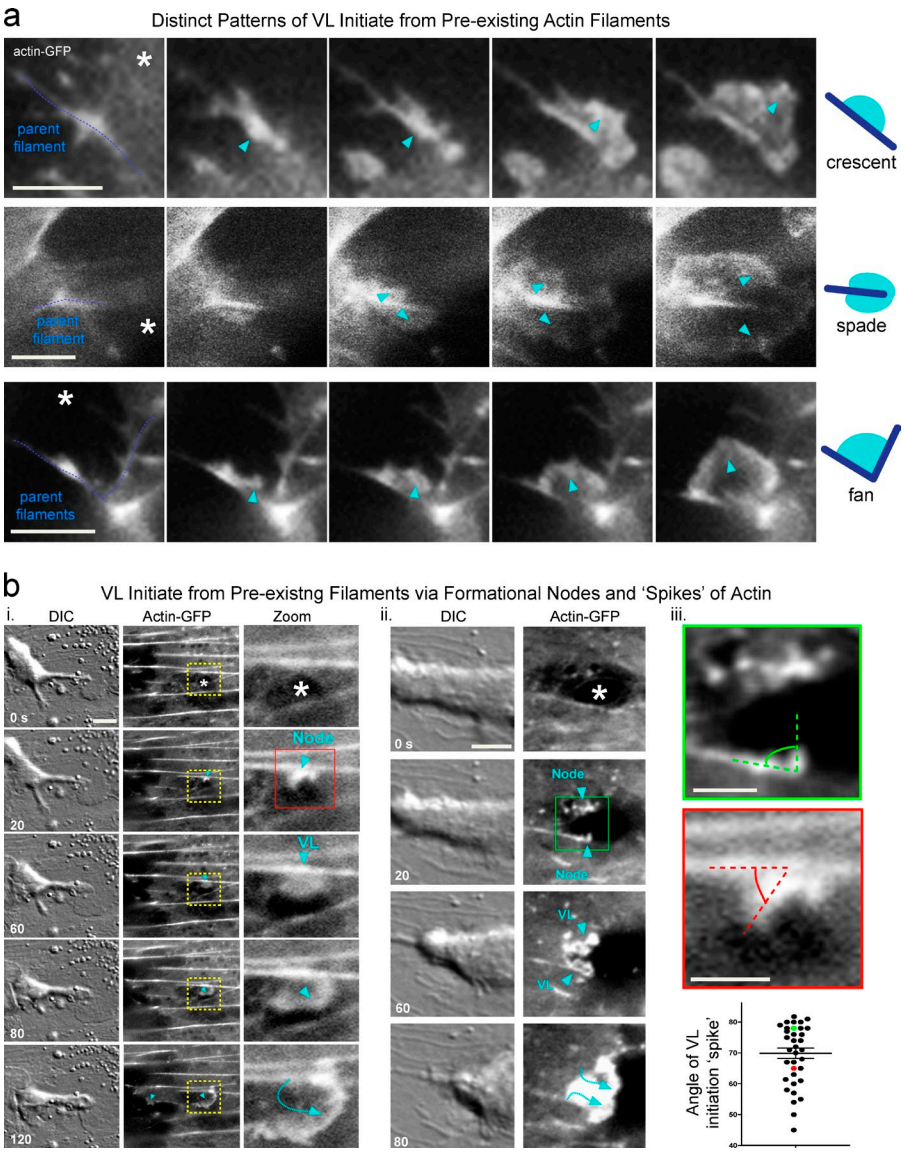

Figure 4. **VL are initiated preferentially from actin filaments.** MVECs expressing actin-GFP were imaged, at 10-s intervals, during the formation of diapedesis micro-wounds (asterisk). (a) Parent filaments (dashed blue line) accumulate and increase actin density that then burst into VL (arrowhead). Three morphologically distinct types of VL initiation types are typically seen: a crescent formed from the side of a filament, a spade whereby actin bursts from both sides of the filament, and a fan born from the intersection of two filaments. (b) Actin initiation nodes/spikes transition to VL with immediate directional adjustment to ensure directed VL radiation into the micro-wound (i and ii, arrowheads and dashed line). (iii) Quantitative analysis of the angle of spike protrusion with respect to its parent spike (representative measurement indicated by green and red dashed lines; $n > 35$). See Video 4. Bars: (a and b, i and ii) 5 µm; (b, iii) 2 µm.

Micromechanical transcellular disruptions promote VL

The aforementioned findings imply that the principal cues driving VL formation and propagation might be mechanical, rather than a result of diapedesis itself. To test this, we designed a system for creating leukocyte-independent mechanical micro-wounds using a tungsten probe (Fig. 6 a). By driving the probe directly across endothelial cells, we could form survivable transcellular micro-wounds in a spatiotemporally controlled manner (Fig. 6 b). Such cell piercing resulted in breakage of adhesions and cytoskeleton, which was coupled to a short-lived phase (~10–40 s) of membrane retraction, whereby the transcellular micro-wound expanded from a diameter of ~1 µm to 28.7 ± 1.4 µm. Within ~20 to ~180 s (mean of ~40 s) of probe micro-wounding, dozens of ~1–3-µm actin enrichment nodes/spikes appeared within the 28.6 ± 2.8-µm radius of the wound edge (Fig. 6 b, arrowheads; Fig. S3 a; and Video 5, Part I). These nodes formed mostly at the ends, or on the side, of radially retracted filaments, but also on tangentially oriented filaments within the retracting network (Fig. 6 b, ii and iii). Such nodes protruded against the underlying substrate as indicated by IRM (Fig. 6 b, ii). They quickly expanded, merged, and coordinately traveled (23.9 ± 3.6 µm at 2.6 ± 0.2 µm/min) toward and across the micro-wound with mixed VL and VW characteristics. Multiple, successive probe-induced transcellular micro-wounds could be efficiently healed in this way (Video 5, Part I). Of note, in contrast to transcellular diapedesis, the probe-mediated transcellular wounds were associated with elevation of intracellular calcium, which was typically reversed in ~10–60 s (Fig. S3, b and c). This suggests that probe micro-wounds involve tearing, followed by rapid repair, of the plasma membrane. Such repair can occur in virtually all cells through a strictly calcium-dependent process (McNeil and Kirchhausen, 2005; Bement et al., 2007). Analysis of calcium flux and VL initiation kinetics on a per-wound basis showed that VL formed only after the reversal of intracellular calcium flux. A subset of cells that failed to normalize calcium failed to form VL (Fig. S3 c, iii). Moreover, pharmacological elevation of calcium at later stages of micro-wound healing caused immediate retraction of the VL (unpublished data). These results suggest that VL do not require

Published April 29, 2013

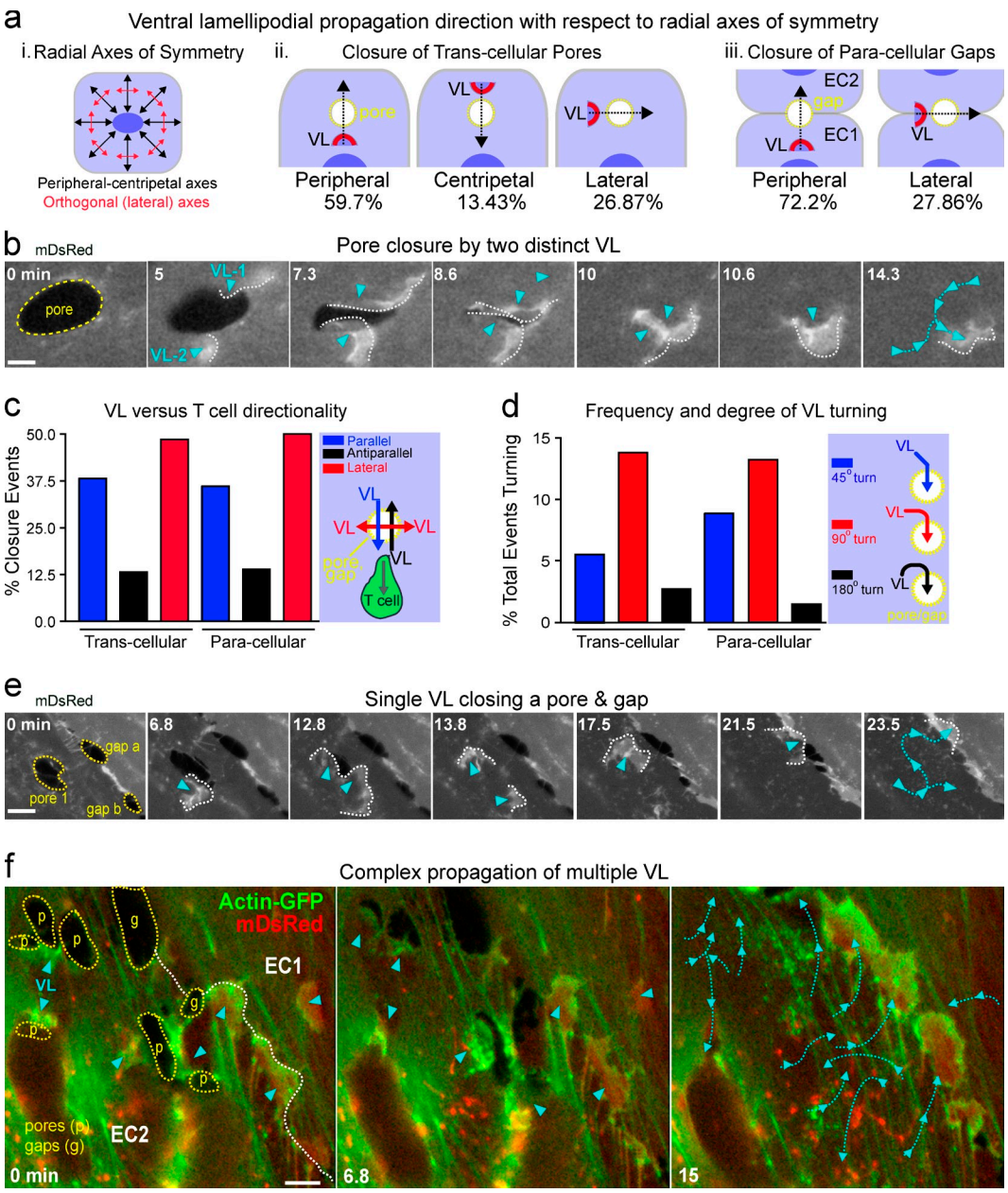

Figure 5. **VL exhibit uniquely directed propagation and steering capacity.** (a) VL directionality with respect to the radial axes of symmetry. (i) Schematic of radial axes (black arrows) spanning between the nucleus (dark blue oval) and the cell periphery and lateral axes that are oriented orthogonally to each radial axis. (ii) Schematic and corresponding frequency of three directional classifications of pore-closing VL and two for gap-closing VL (iii). $n > 10$. (b) Example of pore closure by multiple distinctly directed VL (arrowheads). (c) Percentage of VL that travel parallel, antiparallel, or lateral with respect to T cell migration direction. $n > 35$. (d) The frequency of ∼45°, ∼90°, and ∼180° turns during VL propagation. $n > 100$. (e) VL steering (cyan arrowheads/lines) during successive diapedesis pore/gap (yellow lines) closures. (f) Complex independent directionality of multiple VL (cyan arrowheads/lines) during closure of concomitantly formed diapedesis pores and gaps (p and g, dashed yellow lines). (b–d) See Video 4. Bars, 5 µm.

and, in fact, are inhibited by elevated intracellular calcium. Thus, for endothelial micro-wounds involving membrane damage, membrane repair/cell survival and barrier restoration are sequential, mechanistically distinct processes.

Micromechanical monolayer disruptions promote VL in non-wounded neighbors

Micro-wounding of a cell near its junction caused paracellular gaps to form. Here the directly wounded cell and its untouched/nonwounded neighbor (which did not flux calcium) retracted from each other and then each formed extensive restorative VL/VW emanating specifically from the zones of retraction (Video 5, Part II). We also frequently observed robust VL in nonwounded neighbors in the absence of junction disruption. In such cases, transcellular micro-wound expansion could be relayed to distant (∼5–40 µm) intact junctions, as demonstrated by translation of the unbroken junction in the direction parallel to pore expansion (Fig. 7 a and Fig. S3 d, note green and blue dashed lines; and Video 6). Selectively, at these zones of retraction, unwounded neighbors formed VL that moved toward the

Published April 29, 2013

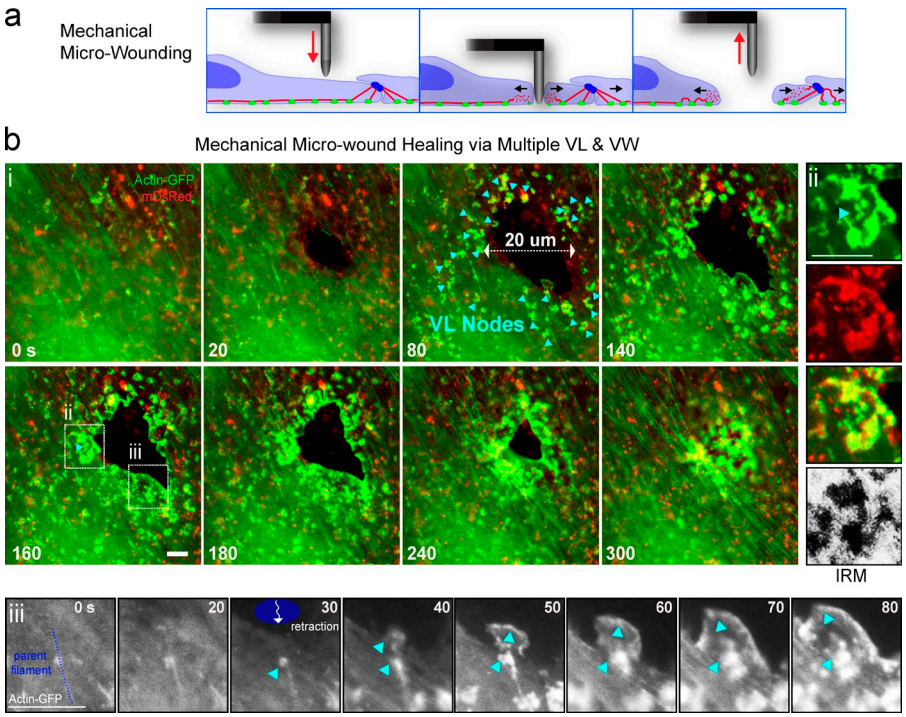

Figure 6. **Endothelial responses to mechanical micro-wounding.** (a) Schematic of a mechanical probe cell micro-wounding apparatus to locally disrupt membrane (blue), cytoskeleton (red), and adhesions (green). (b) Live imaging of MVEC micro-wound formation and healing. (i) Initial wound rapidly expands to ~20 µm diameter (0–80 s). Multiple nodes of individual VL (arrowheads) as well VW form around the pore and propagate toward and across it to restore an intact endothelium. (ii) An individual VL formed adjacent to the wound edge shows doubling of membrane signal and close substrate contacts (IRM). (iii) A parent actin filament (dashed blue line) is shown that is radially oriented with respect to the wound. As the wound expands and the cell locally retracts toward the filament a node of actin accumulates on it and transitions to a VL. See Video 5. Bars, 5 µm.

wound and expanded under the wounded neighbor in similar fashion to cryptic lamellipodia seen in scratch wounding and collective cell migration (Farooqui and Fenteany, 2005; Fig. 7 a, Fig. S3 d, and Video 6). Similar responses were seen in probe-wounded MDCK epithelial monolayers (Fig. S4). Neighbor responses were unaltered by continuous washing (unpublished data), suggesting that these were not regulated by gradients of factors released from the wounded cell. Moreover, similar retraction and response behaviors could also be seen in cells separated from the wounded cell by one or more nonwounded cells (i.e., rough equivalents to "submarginal" cells in scratch wounds; unpublished data). Together our findings suggest that closure of transcellular and paracellular discontinuities, initiated by diapedesis or mechanical probe, involves similar VL/VW mobilization responses and points toward mechanical changes as potential signals for these responses.

A putative tension-loss signal for repair after adhesion rupture

Next, we used our probe-induced micro-wound model to understand how the endothelium perceives perturbations in the mechanical force balance. Specifically we took advantage of the wound-induced cell retractions (i.e., viscoelastic recoil), which are a well-established reflection of local dissipation/relaxation of preformed isometric tension (Kumar et al., 2006; though calcium flux might also contribute to pore expansion in transcellular probe wounding). By placing the probe in different subcellular locations we formed wounds that retracted asymmetrically in one or more zones and showed visible stretching/tensing in adjacent ones. Consistently, retraction areas were the preferred sites of VL formation (Fig. 7 a, Fig. S3 d, and Video 6). Within these areas filaments experiencing the most significant viscoelastic recoil formed actin nodes (Fig. 7, Fig. S3 e, and Video 7). For example, in Fig. 7 b several radially oriented filaments in an untouched cell (blue dashed lines) undergo significant recoil after wounding of a neighboring cell. These then rapidly formed actin nodes that transitioned into VL. Nearby filaments that were more tangentially oriented (Fig. 7 b, magenta lines) and did not recoil failed to form VL (Video 7, ex.1). Additionally, retraction/tension release could be seen to propagate from radial (Fig. S3 e, dashed blue lines) to tangential filaments through cross-links in the actin network. In such cases, both radial and tangential filaments, and often specifically their intersection, formed sites for VL nodes (Fig. S3 e and Video 7, ex. 2). These findings suggest that local loss of tension accompanying adhesion rupture is a key activator of the VL/VW recovery response.

To further test this idea, we pretreated endothelial cells with compounds that block tension development, including the Rho kinase inhibitor Y27632, the myosin light chain kinase inhibitor ML-7, and the myosin II inhibitor blebbistatin. All treatments reduced stress fibers, but left a finer actin network intact (unpublished data). Micro-wounding in the continuous presence of drug resulted in decreased rates of wound expansion/recoil (Fig. 8 a, i), demonstrating that tension was indeed reduced (Kumar et al., 2006). Y27632, which least effectively reduced tension, modestly delayed VL formation (Fig. 8 a, ii) and, as a result, decreased the efficiency of recovery (Fig. 8 a, iii). ML-7 yielded a greater disruption in both tension and VL initiation/recovery efficiency. In both cases, normal VL directionality toward the micro-wounds was preserved. For blebbistatin, which profoundly reduced the isometric tension (Fig. 8 a, i), no VL responses were seen within 20 min of wounding in 15 separate trials. However, unhealthy cell appearance after wounding indicates that cytotoxicity may have contributed to this particular result. Overall, these results suggest that partially dissipating

Published April 29, 2013

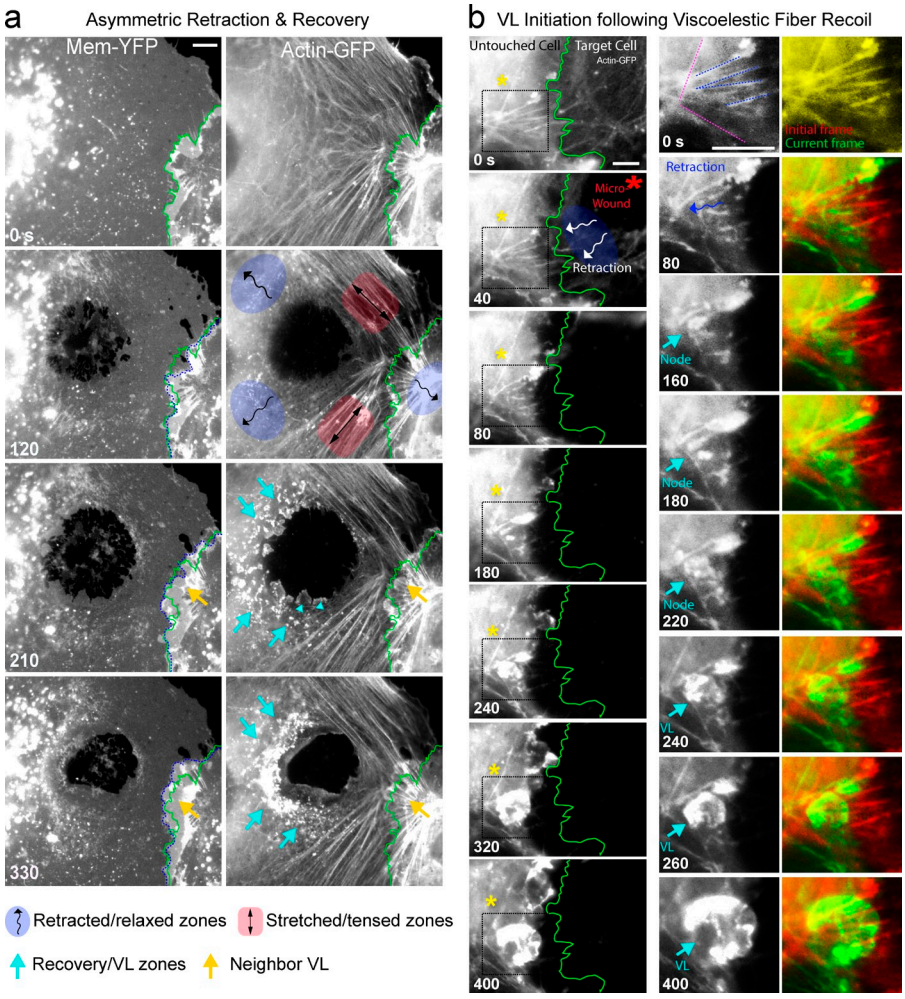

Figure 7. **A putative tension release signal for VL.** (a) Example of asymmetric viscoelastic recoil/relaxation in discrete regions (shaded blue) of MVEC after probe wounding of MVEC. Adjacent untouched filaments undergo visible extension (red shaded areas). Robust VL and VW recovery responses predominantly formed in the relaxed areas (cyan arrows; arrowheads show individual VL). Dashed green and blue lines indicate the original and current position, respectively, of an intercellular junction adjacent to the transcellular micro-wound. At 120 s after wounding significant retraction of the intact junction toward the untouched neighbor is evident. At 210 and 330 s, strong localized VL responses are evident from the neighbor precisely where the initial relaxation occurred (yellow arrow). See Video 6. (b) Zones of viscoelastic recoil (blue shading and curved arrows) in actin networks form nodes of VL initiation on intact filaments. Actin-GFP was imaged in an untouched MVEC immediately before and at indicated times after mechanical micro-wounding of a neighbor cell. Panels on right are zoomed views of the boxed region. Overlay (far right) of the initial (red) and current (green) time points highlights the viscoelastic recoil and shortening of filaments upon broken adhesion with the neighbor. The retracted filaments (blue lines at 0 s) rapidly accumulated actin nodes (cyan arrow) and transitioned to VL that propagated into the micro-wound. Adjacent, nearly orthogonally oriented filaments (dashed magenta lines at 0 s) did not undergo appreciable recoil/retraction or form nodes or VL (left, asterisk). See Video 7. Bars, 5 µm.

isometric tension before micro-wounding blunts the efficiency of VL responses.

Finally, as a complementary test of the role of tension loss in signaling VL, we designed a substrate compression/de-stretch experiment to enforce uniaxial decrease in isometric tension without micro-wounding, adhesion rupture, or generation of free space (Fig. 8 b, i). Thus, endothelial cells were grown on uniaxially prestretched silicone membranes and then imaged during an acute 10% compression of the substrate. Immediately (~30 s) after substrate de-stretch, endothelial cells generated bursts of new lamellar activity preferentially in the direction antiparallel to the compression (Fig. 8 b, ii and iii; and Video 8). This activity was initiated largely at, or just behind, the cell edge typically at the ends of filaments that were at least partially aligned with the axis of de-stretch (Fig. 8, b [iii] and c; and Video 8).

VL are functionally dependent on Rac1, cortactin, and Arp2/3

Based on similarity to migratory leading edge lamellipodia and findings that Rac1 can be modulated positively by tension release (Houk et al., 2012) we examined the role of Rac1 in VL formation. Overexpression of a dominant-negative Rac1, but not RhoA, significantly decreased VL velocity and increased pore/gap closure time after diapedesis (Fig. 9 a). Acute treatment with the Rac1 inhibitor NSC23766 caused immediate arrest of VL (Fig. 9, b and c; and Video 9, Part I). Drug washout resulted in rapid and synchronized mobilization of multiple steered VL that closed the micro-wounds accumulated during drug treatment (Fig. 9, b and c; and Video 9, Part I). Acute addition (contrasting the pretreatment experiment in Fig. 8 a) of the inhibitor Y27632 did not affect VL (Video 9, Part II). GFP fusions of the Rac1 effectors cortactin and IQGAP were dynamically recruited to and enriched in both initiation node and leading edge of VL (Fig. 9, d and e). In contrast, markers for a range of vesicular compartments (e.g., caveolae and endosomes) or microtubules were either not enriched or were excluded from VL (Fig. 9 d). Dominant-negative, but not wild-type, cortactin significantly decreased VL velocity and inhibited diapedesis micro-wound healing (Fig. 9 f). Addition of NSC23766 during probe micro-wounding caused immediate collapse of VL (Fig. 9 g). CK-666, an inhibitor of the Rac1-regulated actin nucleator Arp2/3, also reversibly blocked VL and micro-wound healing (Fig. 9 h).

VL require local p47Phox-dependent production of ROS

Endothelial cell migration and migratory leading edge lamellipodia are regulated by discretely localized production of hydrogen peroxide (H_2O_2) by the Rac1 effector/NADPH oxidase subunit p47phox, which acts in concert with cortactin and IQGAP (Ikeda et al., 2005; Touyz et al., 2005; Moldovan et al.,

Published April 29, 2013

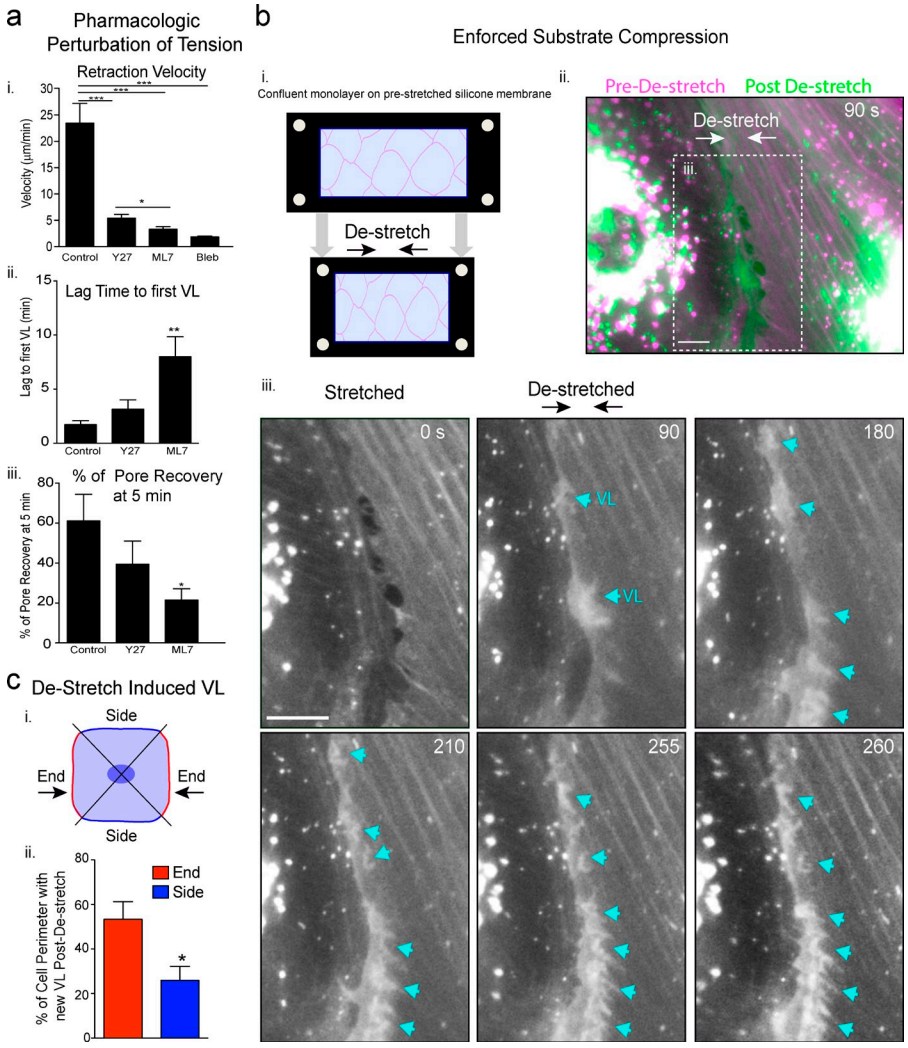

Figure 8. **Probing roles for tension in VL initiation.** (a) MVECs were pretreated with Y27632, ML-7, blebbistatin, or vehicle (control) for 30 min and then subjected to probe micro-wounding in the presence of drug. Velocity of wound retraction (i), time until first appearance of VL (ii), and the percentage of pores recovered by 5 min after wounding (iii) were measured. $n > 15$. (b) Schematic of a uniaxial de-stretch/compression experiment (i). MVEC monolayers expressing actin-GFP and mYFP were grown on 20% prestretched silicone membranes and imaged during an acute 10% de-stretch. An inter-endothelial junction region is shown as either overlay of the stretched (magenta) and 90 s after de-stretch (green) time points (ii) or as sequential time series (iii). Cyan arrows highlight putative VL formed after de-stretch. See Video 8. (c) Analysis of de-stretch–induced VL formation at ends versus sides of cells (Katsumi et al., 2002). $n = 11$. All values are mean ± SEM. Statistical significance is indicated with p-values as follows: ***, $P < 0.001$; **, $P < 0.01$; *, $P < 0.05$. Bars, 5 μm.

2006; Terada, 2006; Ushio-Fukai, 2006). Live imaging showed that p47phox-DsRed was enriched in both the initiation node and leading edge of the VL, as well as in VW-type punctae trailing the leading edge (Fig. 10 a, Fig. S5 a, and Video 10, Part I). Similar enrichment was seen in the VL/VW after probe wounding (Fig. S5 b). To assess H_2O_2 production we used an H_2O_2-selective GFP-based biosensor HyPer (Belousov et al., 2006) and targeted it to the membrane (mHyPer) by addition of a C-terminal farnesylation tag. Imaging of cells expressing mHyper during titration of exogenous H_2O_2 confirmed sensitivity to be in the range of ~100 nM H_2O_2 (Fig. S5 c; Antunes and Cadenas, 2000; Belousov et al., 2006). During diapedesis we consistently detected local increase in H_2O_2 production within pore/gap-closing VL (Fig. 10 b).

We next performed studies with a range of complementary pharmacological disruptors of NADPH oxidase signaling including VAS-2870, diphenylene iodonium (DPI), apocynin, PEG-catalase, and Tempol (Griendling et al., 2000; Drummond et al., 2011). Addition of these inhibitors during leukocyte diapedesis or after probe-induced wounding significantly reduced H_2O_2 and arrested VL/micro-wound healing. Drug washout rapidly reversed this effect (Fig. 10, d and e; Fig. S5 e; and Video 10, Part II). Together, our findings show that in response to mechanical cues the endothelium uses discretely regulated Rac1 and NADPH oxidase signaling that coordinates unique actin remodeling dynamics to heal disruptions in its barrier.

Discussion

This study was designed to investigate the mechanisms that complete diapedesis and restore endothelial barrier integrity. Although providing an answer to this question, our findings unveil basic mechanisms for tissue homeostasis with potentially broad relevance. We reveal VL as a novel type of actin remodeling in endothelia and epithelia that is distinct from known lamellipodia or dorsal ruffles (Chhabra and Higgs, 2007) and serves to close diapedesis pores/gaps. VL are nucleated from preexisting actin filaments and exhibit the unique ability to propagate under cells independently of radial axes of cell symmetry and to dynamically change direction in response to additional discontinuities. These findings raise important new questions about fundamental mechanisms for nucleation of actin assemblies and coordination of their propagation, which point toward interesting roles for mechanotransduction.

We hypothesized that transcellular diapedesis micro-wounds might be healed by purse strings that heal seemingly similar

Published April 29, 2013

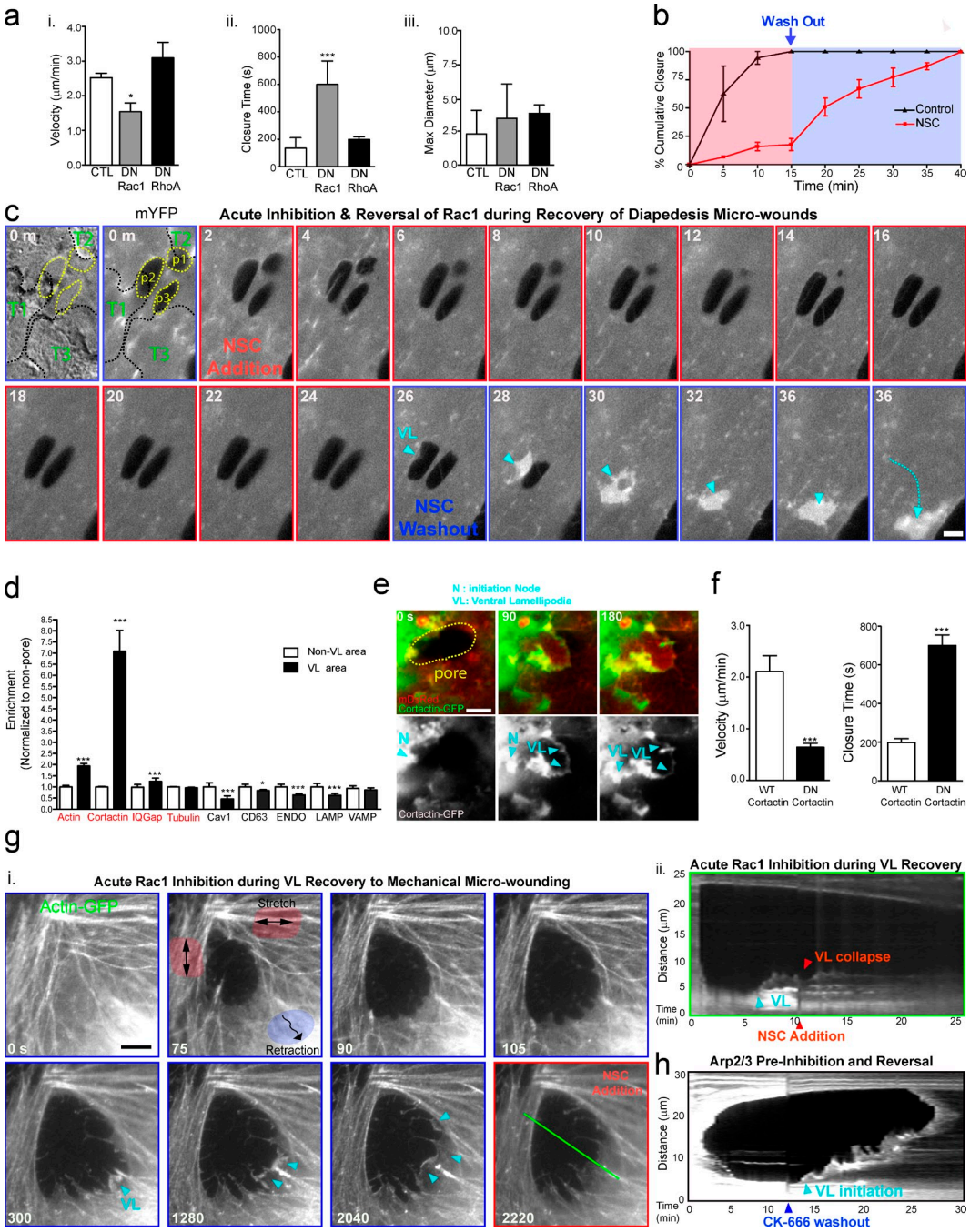

Figure 9. **VL depend on Rac1, cortactin, and Arp2/3.** (a) MVECs were coexpressing mDsRed and GFP dominant-negative Rac1 (DN Rac1) or Rho A (DN RhoA) and imaged during T cell diapedesis. VL velocity (i), wound closure time (ii,) and diameter (iii) were measured. (b) MVECs expressing mYFP were imaged during T cell diapedesis and addition of Rac1 inhibitor NSC23766 or vehicle (red phase) and after drug washout (blue phase). The cumulative percentage of wound closure was plotted as a function of time. $n = 5$. (c) A representative imaging of reversible VL blockade. (top left) Two DIC and mYFP panels show three transcellular pores recently vacated by T cells (T1–T3). Subsequent panels are after addition (red outline) or washout (blue outline) of NSC23766. Arrowhead indicates pore closing VL rapidly mobilized after washout. See Video 9. (d) MVECs coexpressing mDsRed and GFP-fused actin, cortactin, tubulin, Caveolin-1, CD63, Lamp1, VAMP2, and an endosomal marker (ENDO) were imaged during T cell diapedesis. mDsRed-normalized intensities of each GFP construct were quantified in VL versus non-VL regions. $n > 5$. (e) Representative images of cortactin enrichment both in initiation nodes (N) and VL leading edges (VL; arrowheads). (f) VL velocity (i) and diapedesis wound closure time (ii) in MVECs expressing wild type (WT) or dominant-negative cortactin-GFP (DN). All values are mean ± SEM. Statistical significance is indicated with p-values as follows: ***, $P < 0.001$; *, $P < 0.05$. (g, i) Actin-GFP–expressing MVECs were mechanically micro-wounded. VL (arrowheads) that formed specifically in zones of recoil (blue shading) and collapsed upon addition of NSC23766. Green line traces location used for kymograph of this process (ii). (h) Kymograph of MVECs micro-wounded in the presence of Arp2/3 inhibitor CK-666, and VL (cyan arrowhead) initiation after drug washout. $n = 10$. Bars, 5 μm.

single-cell wounds in other settings (McNeil and Kirchhausen, 2005; Bement et al., 2007). However, in sharp contrast to purse strings, pores were closed through an asymmetric propagation of actin via a calcium-, Rho-, and tubulin-independent mechanism. Though transient calcium flux (and membrane tear and repair) was evident in probe-generated single endothelial cell

Published April 29, 2013

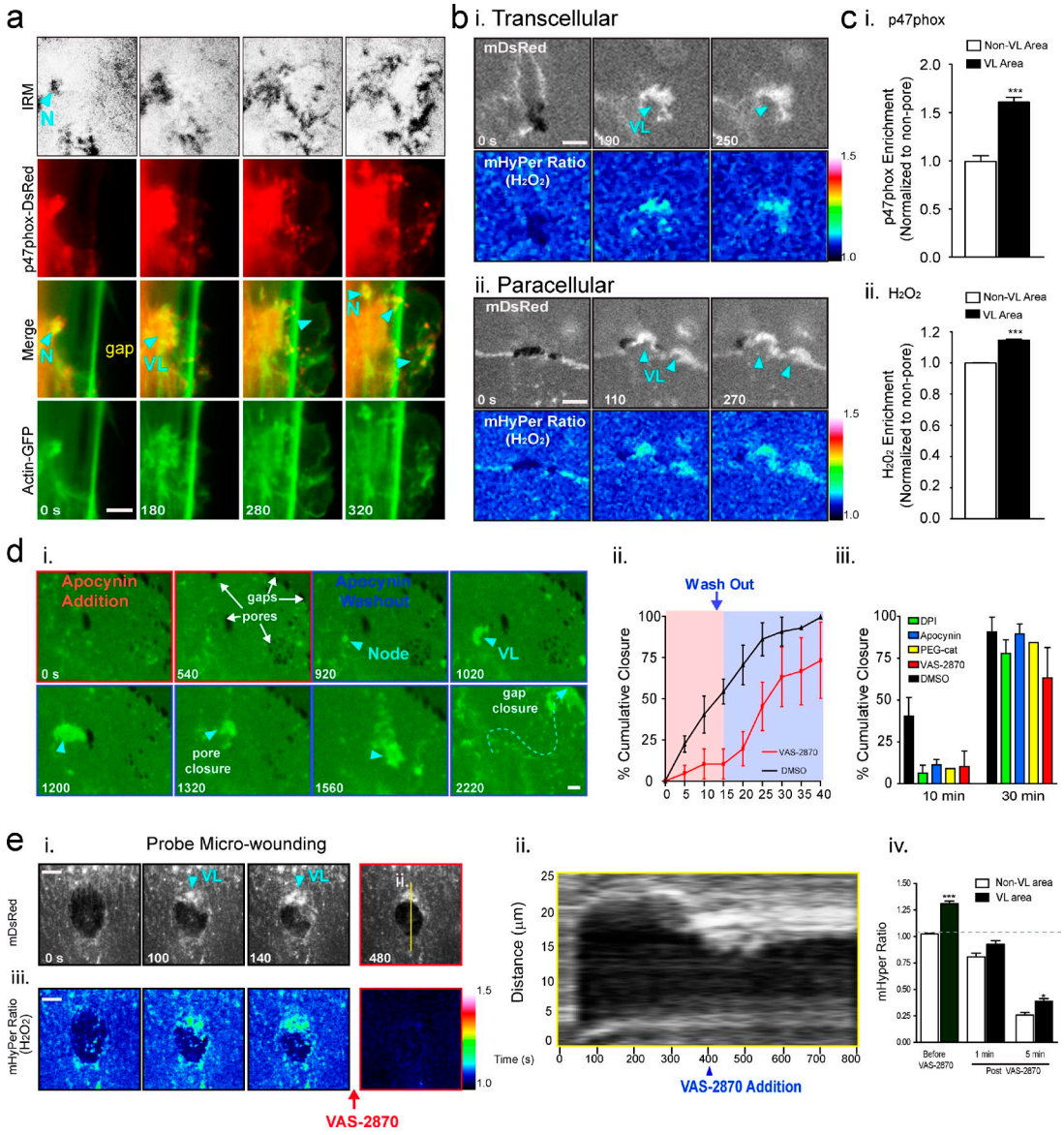

Figure 10. **VL are enriched in and functionally dependent on NADPH oxidase activity.** (a) MVECs coexpressing p47phox-DsRed and actin-GFP were imaged live during T cell diapedesis. p47phox was enriched in ventral (IRM) actin-rich initiation nodes (N) and in VL leading edge (arrowheads). See Video 10. (b) Representative ratiometric images of H_2O_2 production in (i) pore- and (ii) gap-closing VL in MVECs expressing the biosensor mHyPer during T cell diapedesis. (c) Quantification of p47phox (i) and H_2O_2 (ii) enrichment in VL. $n > 13$. (d, i) Representative NADPH oxidase inhibition/washout imaging experiment. After multiple T cell diapedesis events on MVECs expressing mYFP, apocynin was added. Arrows indicate multiple pores and gaps that persisted for 15 min, but were rapidly healed by steered VL (arrowheads) after drug washout. See Video 10. Experiments as in d (i) were performed with VAS-2870, DPI, PEG-catalase, and DMSO (control) and quantified by cumulative wound closure analysis, shown as a continuous line plot (ii) and bar graph of single pre/post-washout time points (iii). $n > 5$. (e) MVECs coexpressing mDsRed and mHyPer were imaged during probe wounds and after addition of VAS-2870. Representative mDsRed images (i), kymograph (ii), mHyper ratiometic images (iii), and quantitation (iv) are shown. $n = 3$. Values represent mean ± SEM. Statistical significance is indicated with p-values as follows: ***, $P < 0.001$; *, $P < 0.05$. Bars, 5 µm.

wounds, these pores also closed through VL. This different response is likely related to distinctions in cell morphology and function. Contractile rings are seen after wounding of large spherical cells (e.g., *Xenopus laevis* oocytes), where they function to restore the cortical cytoskeleton of individual cells. On the contrary, endothelial cells are thin and flat and function collectively as a barrier. VL might, thus, be favored for closing transcellular wounds in endothelia as a contractile process would be liable to disrupt the barrier elsewhere (i.e., promote paracellular gaps; Wojciak-Stothard and Ridley, 2002). Moreover, as a calcium-independent activity, VL can respond to diverse para- and transcellular discontinuities whether or not plasma membrane damage is involved.

The preceding discussion raises the fundamental question of how discontinuities are perceived by barrier cells. Intact endothelia and epithelia exist under isometric tension in which contractile forces are balanced by cell–matrix and cell–cell adhesion (Chicurel et al., 1998; Vogel and Sheetz, 2006; DuFort et al., 2011; Gomez et al., 2011). The process of diapedesis involves intricate leukocyte protrusive dynamics that cause breakage of cell–cell and cell–matrix adhesions and distortions of membrane and cytoskeleton in endothelia/epithelia (Chin and

Published April 29, 2013

Parkos, 2007; Ley et al., 2007; Carman, 2009a). We envisioned that the nodes of VL initiation would likely coincide with hotspots of maximal changes in forces felt by the endothelial and epithelial cells. Because of the multiplicity and small size of diapedesis pores and gaps, measurement of their force landscapes and associated signaling mechanisms is difficult. We therefore developed a probe-induced micro-wounding model with more tractable force change dynamics.

Probe-induced transcellular micro-wounding showed that subcellular regions of retraction correlated with zones of VL initiation. Such retraction can be taken as a well-established readout for dissipation of the preexisting isometric tension (Rajfur et al., 2002; Kumar et al., 2006; Ma et al., 2009; Murrell et al., 2011). In cases of asymmetric retraction, adjacent nonretracting regions/filaments showed little VL response. Importantly, recoil transferred from a wounded cell to a nonwounded neighbor through discrete segments of intact junction produced avid and localized VL responses in the neighbor. This result suggested that no direct cell damage, intercellular adhesion rupture, or generation of free space was necessary to stimulate VL. Similar experiments done with continuous media perfusion ruled out chemical gradients in driving these neighbor responses. We therefore hypothesized that the localized decrease in tension (i.e., force unloading) associated with micro-wounding provides a primary positive signal for VL formation. This was supported by our finding that dissipating tension pharmacologically before wounding resulted in both slower recoil and slower VL initiation. Conversely, acute imposition of uniaxial tension release through substrate compression promoted rapid VL-type responses that were biased toward the direction of tension loss. This latter experiment, that is completely independent of wounding or free space generation, provides particularly strong evidence that tension loss can provide a direct cue to initiate the recuperative response.

Such a tension-based model helps to explain how VL can respond from a distance and participate in both transcellular and paracellular micro-wound closure (as broken tension is transmitted throughout the monolayer [Gomez et al., 2011]). The findings that nascent VL rapidly tweak their orientation of growth to ensure movement toward the micro-wounds and that mature VL can further adjust their directionality in response to additional discontinuities suggest that biomechanical and/or biochemical feedback exists. One possibility is that the low-tension zone created by the micro-wound is simply permissive for continued VL propagation, whereas adjacent zones of higher (i.e., basal) tension are not, creating a funnel effect. This would be consistent with the observed steering toward new wounds (as a new trench redirects water flow) and the quenching of VL after completion of wound healing, which presumable restores basal tension.

Existing paradigms for tissue mechanobiology focus on how force loading of sensitive elements within cells (e.g., integrins, actin filaments, and ion channels) triggers protective remodeling responses that help cells resist rupture of adhesions, of the cytoskeleton, and of the plasma membrane (Orr et al., 2006; Vogel and Sheetz, 2006; Geiger et al., 2009; DuFort et al., 2011; Gomez et al., 2011; Sinha et al., 2011). Our study provides highly physiological examples of what happens when ruptures ultimately occur. Importantly, similar VL recuperative responses were seen in endothelia and epithelia after both leukocyte- and mechanical probe–induced micro-wounding. These findings extend and complement the field of mechanobiology, offering new ways to think about how cells/tissues perceive mechanical information and how they monitor and respond to changes in integrity.

Permutations of this phenomenon will likely have relevance for diverse adhesion and cell ruptures. For example, physiological extremes in shear and/or stretch cause constitutive tearing of aortic and skin endothelia, which seem to be repaired efficiently by incompletely characterized mechanisms (McNeil and Ito, 1990; Yu and McNeil, 1992). Our findings also have implications for collective cell migration during tissue wound healing, angiogenesis, and development. A hallmark of this process is that followers (e.g., submarginal cells of a tissue wound) migrate actively in coordination with the leaders. It is proposed that mechanical tension or "tugging" transmitted through intercellular adhesions is critical to stimulate polarization and cryptic lamellipodia in submarginal cells (Farooqui and Fenteany, 2005; Friedl and Gilmour, 2009; Tambe et al., 2011). However, this seems somewhat inconsistent with findings that lamellar activity is potently suppressed by tension (Kolega, 1986; Raucher and Sheetz, 2000; Katsumi et al., 2002; Shifrin et al., 2009; Ehrlicher et al., 2011; Gauthier et al., 2011; Houk et al., 2012). Our studies instead predict that extremes in tension could result in localized adhesion ruptures and that the released tension would drive new lamellar bursts that effectively spur lagging followers to catch up. This is consistent with the finding that, indeed, endothelial and epithelial migrations follow local orientations of maximal principal stress (Tambe et al., 2011) and that gaps are seen frequently in collective migration studies. Based on empirical observations, the idea that cycles of gap formation and lamellar closure could drive collective migration has been proposed before but in terms of regulation by free space rather than tension (Radice, 1980). Our nonwounded neighbor and substrate compression studies suggest that the former, but not the latter, is dispensable for VL initiation.

The principle of tension breakage driving actin polymerization is supported by observations in disparate systems. Mechanical rupture of actin gels growing on beads creates local tension release that drives the physicochemical enhancement of actin assembly and comet formation (Paluch et al., 2006). The ends of broken filaments similarly provide a direct source of free barbed ends available for new growth (Chhabra and Higgs, 2007), as was evident to varying degrees during probe- and diapedesis-induced micro-wound healing. Unbroken actin filaments and filament segments upstream of a break, which we observed as prominent VL nucleation sites, can also serve as conformation-based tension sensors by differentially binding distinct function-modifying proteins under low versus high strain (Galkin et al., 2012). Integrins, which were critical for VL propagation, are also excellent candidates as mechanosensors of micro-wounding (Orr et al., 2006; Geiger et al., 2009). Whatever the ultimate initiation cue, our studies show that VL are strongly dependent on Rac1 activity, which is known to undergo spatially restricted and reversible repression in response to tension

Published April 29, 2013

(Kolega, 1986; Raucher and Sheetz, 2000; Katsumi et al., 2002; Gauthier et al., 2011). It was shown recently that acutely releasing tension in the uropod of migrating neutrophils produced rapid derepression of Rac1 that was coupled to new bursts of leading edge lamellipodia (Houk et al., 2012). We postulate that our studies recapitulate such results, but in the context of a cell monolayer and with the function of restoring integrity rather than promoting cell migration. New findings that the Rac1 inhibitor FilGAP is rapidly sequestered by filamin A (an actin cross-linking protein) upon release of actin network tension provide at least one plausible molecular mechanism for such events (Shifrin et al., 2009; Ehrlicher et al., 2011).

Downstream of Rac1, VL critically depended on Arp2/3, as well as discrete local production of ROS, specifically H_2O_2, which is driven by coordinated function of cortactin, IQGAP, p47phox, and likely NOX2. Indeed, a range of antioxidants/inhibitors of H_2O_2 caused profound disruption of VL responses. Interestingly, H_2O_2 has been shown recently to stimulate lamellipodia by recruiting Arp2/3 (Taulet et al., 2012). Thus, whereas oxidative stress and excessive ROS production are generally viewed as harmful to tissues (Griendling et al., 2000; Lum and Roebuck, 2001; Rodrigues and Granger, 2010; Drummond et al., 2011; Browning et al., 2012), our studies define a specific protective/homeostatic role for ROS in the maintenance of tissue integrity. The rapid production, short half-life, and limited diffusion distance of H_2O_2 makes it particularly well suited, when formed at low levels, for regulating complex subcellular dynamics such as those of VL micro-wound healing (Terada, 2006).

Collectively, our work illustrates that the barrier function of the endothelium relies on an enormous self-restorative capacity rather than structural robustness. Inherent in this idea is an ability to effectively monitor and respond to local barrier disruptions. This investigation points toward a putative role for broken tension and force unloading as a critical signal of adhesion or cell rupture that is coupled to newly appreciated ROS-dependent recuperative actin dynamics. These findings suggest new concepts for how pathological breakdown of tissue barriers may occur. Whereas excessive disruptive inputs are usually targeted as culprits in vascular dysfunction, failure of the normal homeostatic remodeling could be equally important.

Materials and methods

Antibodies and reagents

The function-blocking anti-αvβ3 and -α5β3 integrin antibodies LM-609 and P1D6, respectively, were obtained from EMD Millipore and used at 20 µg/ml. Inhibitors of Rho signaling used included NSC27632 (inhibitor of TIAM/TRIO activation of Rac1; 500 µM; EMD Millipore), Y27632 (Rho kinase inhibitor; 90 µM; Sigma-Aldrich). The modulator of intracellular calcium, thapsigargin (2 µM), was purchased from Sigma-Aldrich. Inhibitors of cytoskeletal tension included Y27632, ML-7 (the myosin light chain kinase inhibitor; 10 µM; R&D Systems), and blebbistatin (Myosin-II inhibitor; 10 µM; Sigma-Aldrich). Specific inhibition of Arp2/3 was accomplished with CK-666 (100 µM; Sigma-Aldrich). Inhibitors of NADPH oxidase signaling used included VAS-2870 (Nox2/4 inhibitor; 15 µM; Enzo Life Sciences), DPI (non-specific Nox inhibitor/Flavoprotein inhibitor; 12.5 µM; Sigma-Aldrich), apocynin (inhibitor of p47phox assembly into Nox complex/H_2O_2 scavenger; 1 mM; Sigma-Aldrich), PEG-catalase (H_2O_2 degrading enzyme; 200 U/ml; Sigma-Aldrich), and Tempol (superoxide dismutase/catalase mimetic; 500 µM; Sigma-Aldrich). Lipid dye R18 (Octadecyl Rhodamine B) was obtained from Life Technologies.

Cell culture

Studies of human blood were approved by the institutional review board at the Beth Israel Deaconess Medical Center, Harvard Medical School. Preparation of primary human blood cells was performed as described previously (Carman et al., 2003; Carman and Springer, 2004). In brief, granulocytes and peripheral blood mononuclear cells were separated from whole blood by standard Ficoll-Hypaque (Sigma-Aldrich) buoyant density centrifugation. Granulocytes were further purified from contaminating red blood cells by hypotonic lysis, resuspended in HBSS supplemented with 1 mM $CaCl_2$ and $MgCl_2$, 20 mM Hepes, pH 7.4, and 1% human serum albumin (buffer A), and used immediately. Monocytes and lymphocytes were each isolated from PBMC with negative selection isolation kits (Miltenyi Biotec). Monocytes were maintained in buffer A and used immediately. Effector T lymphocytes were generated by culturing T cells in RPMI supplemented with 10% FBS and 1 µg/ml PHA for 3 d, followed by culture in 20 ng/ml IL-2 for 3–6 d. Flow cytometric analysis demonstrated that these cells were 97% CD3 positive. Primary human dermal, lung, and cardiac microvascular endothelial cells and human umbilical vein endothelial cells (Lonza) were cultured on 20 µg/ml of fibronectin-coated substrates and maintained in EBM-2MV media as described previously (Carman et al., 2007). CHO epithelial cells stably transfected with ICAM1-GFP were generated and cultured as described previously (Carman et al., 2007). MDCK epithelial cells were obtained from American Type Culture Collection.

Plasmids and transfections

mYFP, mDsRed, pEGFP-actin, pEGFP-tubulin, and pAcGFP1-Endo plasmids were purchased from Takara Bio Inc. The GFP-based ratiometric H_2O_2 biosensor HyPer was obtained from Evrogen. Membrane-targeted DsRed was generated by overlap-extension PCR to add an N-terminal palmitoylation sequence. Membrane-targeted Hyper was generated by two rounds of site-directed mutagenesis followed by insertion of the farnesyl group through unidirectional subcloning. Other DNA constructs were gifts from P. Turowski (VE-cadherin-GFP; University College London, London, UK), K. Burridge (Rac1N17-GFP and RhoAN19-GFP; University of North Carolina, Chapel Hill, NC), F.W. Luscinskas (cortactin-GFP and cortactin3F-GFP; Brigham and Women's Hospital, Boston, MA), L. Terada (p47phox-DsRed; University of Texas Southwestern Medical Center, Dallas, TX), T. Kirchhausen (CD63-GFP and LAMP1-GFP; Immune Disease Institute, Boston, MA), M. Lisanti (Caveolin-1-GFP; Thomas Jefferson University, Philadelphia, PA), E. Masuda (VAMP2-GFP; Rigel Pharmaceuticals, San Francisco, CA), and B. Werle-Haller (integrin β3-GFP; University of Geneva, Geneva, Switzerland). Integrin α5-GFP and Arp3-GFP were purchased from Addgene. MVEC transient transfection was done by Nucleofection according to the manufacturer's instructions (Amaxa Inc.). Experiments were conducted 48–72 h after transfection.

Leukocyte transendothelial migration

Live-cell imaging of leukocyte diapedesis was performed as described previously (Carman et al., 2007). In brief, confluent monolayers of transfected MVECs were grown on fibronectin (20 µg/ml)-coated Delta-T live-cell imaging dishes (Bioptechs) and stimulated for 24 h with 10 ng/ml TNF. MVECs were washed twice and imaged in buffer A and maintained at 37°C. Lymphocytes, monocytes, or granulocytes were pelleted and resuspended in buffer A and then added to endothelial cell monolayers and subject to live-cell time-lapse imaging (see Epifluorescence, TIRF, and spinning disk confocal microscopy). In all cases, selected imaging fields contained intact confluent endothelial monolayers. However, because transfection efficiencies are typically 30–60%, fluorescent transfectants were variously neighbored by fluorescent and nonfluorescent MVECs. For some experiments function-blocking antibodies or pharmaceutical agents were added during leukocyte diapedesis and, as indicated, subsequently removed by washing five times with buffer A. For select studies, leukocyte–endothelial cell interactions were performed under physiological laminar fluid shear flow using an FCS2 parallel plate flow chamber (Bioptechs) as described previously (Carman et al., 2007). In brief, MVEC monolayers were assembled as the lower wall in a parallel-wall flow FCS2 chamber, which was then perfused with buffer A at 37°C using a syringe pump (Harvard Apparatus). Leukocytes in buffer A were infused at 0.3 dyne/cm^2 for 30 s to allow accumulation, and then were subjected to 4 dyne/cm^2 shear force during continuous live-cell imaging at 37°C.

Epifluorescence, TIRF, and spinning disk confocal microscopy

All live-cell time-lapse imaging was performed at 37°C in buffer A with 10–60-s intervals using the following fluorochromes: GFP, YFP, DsRed, HyPer, Fura-2, and Cy5. Epifluorescence, differential interference contrast (DIC), and IRM were performed on a microscope (Axiovert 200M; Carl Zeiss)

Published April 29, 2013

equipped with a camera (Orca charge coupled device [CCD]; Hamamatsu Photonics) using a 40× Plan-Neofluar (NA 1.3) or 63× Plan-Apochromat oil immersion objective (NA 1.4) and Axiovision 4.6.3 software (Carl Zeiss). TIRF microscopy was performed as described previously (Massol et al., 2006) using a microscope (Axiovert 200M) equipped with a 100× TIRF α-Plan-Fluor oil immersion objective (NA 1.45). A computer-controlled TIRF slider was used to align the laser beams at an off-axis position with an angle of incidence above the critical to achieve total internal reflection. The combination of optical components of this system allows for simultaneous acquisition of green and red fluorophores in either TIRF or wide-field modes. Spherical aberrations were corrected with a computer-driven SAC device (Intelligent Imaging Innovations). Images were acquired with a camera (Cascade 512B; Photometrics) and Slidebook 4 acquisition software (Intelligent Imaging Innovations). Spinning-disk imaging was conducted as described previously (Ehrlich et al., 2004). In brief, images were acquired with a spinning disk confocal head (PerkinElmer) coupled to a microscope (Axiovert 200M) equipped with a 63× α-Plan-Apochromat oil immersion objective (NA 1.46). Images were acquired with a camera (Cool Snap HQ CCD; Photometrics) and Slidebook 4 acquisition software.

Calcium imaging

Endothelial cells were loaded with Fura-2 AM (2 µg/ml; Molecular Probes) for 30 min at 37°C, washed with buffer A, and imaged live during both leukocyte diapedesis and mechanical micro-wounding. To conduct ratiometric calcium flux analysis, a time series of 510-nm fluorescence images were captured after sequential excitation at 340 and 380 nm for each time point using standard Fura-2 filters (Chroma Technology Corp.) and a 40× Plan-Neofluar (NA 1.3) objective. Ratiometric calcium flux was calculated (340nmEX:510nmEM-background/380nmEX:510nmEM-background) for each cell using Axiovision as previously described (Sage et al., 2012). 2 µM thapsigargin (Sigma-Aldrich) was added to samples as indicated as a positive control.

Imaging of intracellular H_2O_2

For imaging of intracellular H_2O_2, MVECs transfected with the mHyPer-GFP biosensor were sequentially excited at 488 nm while reading emission at 420 and 500 nm. Ratiometric H_2O_2 production was calculated (488_{nm} EX:500_{nm}EM-background/420_{nm}EX:500_{nm}EM-background) in the VL leading edge (the 1-µm zone behind the VL leading edge) and in neighboring non-VL areas. To (roughly) calibrate the signal, images were taken during stepwise titration of exogenous H_2O_2 and the calculated ratios were plotted against the corresponding added H_2O_2 concentration. Based on the established gradient of exogenous versus intracellular H_2O_2, applied H_2O_2 concentrations were divided by a factor of 7 to approximate the intracellular concentrations achieved (Antunes and Cadenas, 2000; see Fig. S5 c). Additional validation of the selective sensitivity of mHyPer to H_2O_2 was established by quenching basal H_2O_2 production in MVECs with VAS-2870 (see Fig. S5 d), DPI, apocynin, PEG-catalase, or NSC23766 (not depicted). This analysis showed that all drugs significantly reduced mHyper ratios without affecting mDsRed fluorescence intensity.

Mechanical micro-wounding

A tungsten probe with a 700-nm-diameter tip (The Micromanipulator Co., Inc.) was mounted on a micromanipulator (oriented orthogonally to the imaging plane) and placed directly above an imaging chamber containing an endothelial monolayer (see Fig. 6 a). During live-cell imaging, micro-wounds were generated by briefly (<1 s) driving the tip through the endothelium and into contact with the underlying glass substrate, and then fully retracting it. In some cases cells were treated with a range of pharmacological agents either before or after micro-wounding with or without subsequent drug washout, as indicated.

Endothelial cell de-stretching/compression

Silicone cell culture chambers (3 × 3 cm) were mounted onto a manual stretcher (Strex; B-Bridge International, Inc.), subjected to a 20% uniaxial stretch, and coated for 4 h at 37°C with 100 µg/ml fibronectin. Transfected endothelial cells were then plated on prestreched chambers and cultured for 48–72 h, allowing a stable monolayer to form. Chambers were then mounted onto an inverted microscope and imaged continuously during application of an acute (i.e., over a 1-s interval) 10% unstretch/compression to cause an acute uniaxial drop in the preexisting isometric tension. To accommodate the linear translation and z-axis drift caused by de-stretching, field of view and focus was quickly readjusted (typically within 20–30 s) before resuming image acquisition. Offline analysis included digital alignment of the pre- and post-stretch images followed by peripheral lamellipodia analysis as previously described (Katsumi et al., 2002). Specifically, individual cell perimeters were divided into quadrants to define the cell sides that were oriented parallel to the axis of de-stretch versus the cell ends in the perpendicular orientation (see schematic in Fig. 8 c, i). We then measured the side and end perimeter lengths that exhibited new lamellar activity and expressed them as a fraction of total side and end perimeter lengths. This was repeated for multiple cells in multiple experiments.

Image processing and analysis

All analysis was conducted using Axiovision 4.6.3 and ImageJ software. Morphometric and dynamic features, including VL/VW width, propagation velocity, lifetime distance traveled, and directionality were performed with the aid of the Axiovision Manual Cell Tracking Module and through direct tracing and measurement of VL outlines in sequential frames. To assess VL propagation directionality, a vector was established from sequential frames by connecting the VL initiation site and the final position before being extinguished. The VL vector was compared both with the radial axes of the endothelium (established by drawing a line from the center of the nucleus through the micro-wound toward the cell periphery) and the leukocyte migration vector. VL that exhibited change in direction were characterized by tracking propagation in sequential video frames (using the center point of the leading edge outline as a guide) and quantifying turns in the resulting track with the Axiovision angle measurement tool. For membrane folding analysis, ROIs were drawn around actin-GFP–defined features (i.e., VL- or VW-type structures), as well as adjacent control areas. The mean fluorescence intensity of the corresponding, background-subtracted mDsRed images were then calculated for each VL or VW and normalized to control area for at least 10 separate events. VL enrichment analysis was conducted in MVECs coexpressing mYFP or mDsRed and a fluorescent fusion protein of interest. Background-subtracted mean fluorescence intensities for the protein of interest and for the membrane were obtained in ROIs representing the VL (defined by the 1-µm zone behind the VL leading edge) and non-VL areas. Fluorescence intensities of the protein of interest within VL were first normalized to the membrane signal and then to the corresponding (i.e., membrane normalized) control region. At least 10 separate events were measured for each analysis. Pearson's analysis was performed on background-subtracted images using the Axiovision colocalization module. Inhibition studies were assessed by direct measurement of VL propagation velocities and time required to close a pore/gap starting from the moment at which the leukocyte completely exited it. Alternatively, the percentage of pore/gaps in an imaging field that closed over time was expressed cumulatively. Kymographs were generated using ImageJ software.

Transmission electron microscopy

Transmission electron microscopy was performed as described previously (Carman et al., 2007). In brief, TNF-activated endothelial cells grown on fibronectin-coated coverglass were incubated with T cells for the indicated times and then fixed with 2.5% glutaraldehyde and 2% paraformaldehyde in 1.0 M sodium cacodylate buffer, pH 7.4, for 2 h, post-fixed in 1.5% symcollidine–buffered OsO_4 for 1 h, stained en bloc with uranyl acetate, dehydrated in alcohol, and embedded in eponate. Thin eponate sections of 90 nm were cut with an ultramicrotome (Leica) and visualized with an electron microscope (CM-10; Philips) at an acceleration voltage of 60 KV. Images were taken on negative films. After development, the negative films were subjected to image scanning (using an Epson GT-X978 scanner and Epson File Manager software) and saved as tif files. Image brightness and contrast were adjusted in Adobe Photoshop software (CS4) and T cell and endothelial cell regions were highlighted with 15% opacity blue or green overlay, respectively, in Adobe Illustrator.

Statistical analysis

Results were presented as mean ± SEM for $n \geq 3$. P-values were calculated via Student's *t* tests in GraphPad Prism. Statistical significance is indicated with p-values as follows: ***, $P < 0.001$; **, $P < 0.01$; *, $P < 0.05$.

Online supplemental material

Fig. S1 shows the classification of pore closure events in diverse settings. Fig. S2 shows that VL coexist with VW in endothelial cells. Fig. S3 shows tension breakage and VL responses after mechanical micro-wounding in endothelial cells. Fig. S4 shows tension breakage and VL responses after mechanical micro-wounding in epithelial cells. Fig. S5 shows enrichment of p47phox in VL, validation of mHyper, and inhibition of VL by VAS-2870. Video 1 shows that leukocyte-driven endothelial micro-wounds are closed efficiently. Video 2 shows examples of three classes of pore-closing lamellipodia in diverse settings. Video 3 shows time-lapse spinning disk confocal imaging demonstrating that pore closing lamellipodia form on the ventral surface of endothelial cells. Video 4 shows that VL are initiated from preexisting actin

filaments and exhibit complex propagation features. Video 5 shows examples of closure events after transcellular and paracellular mechanical micro-wounding. Video 6 shows asymmetric cellular retraction and recovery after mechanical micro-wounding. Video 7 shows that tension release correlates with VL initiation on actin filaments. Video 8 shows that enforced substrate compression can initiate formation of putative VL. Video 9 shows differential roles for Rac-1 and Rho-kinase in VL formation and pore closure. Video 10 shows the enrichment of, and functional requirement for, p47phox in VL. Online supplemental material is available at http://www.jcb.org/cgi/content/full/jcb.201209077/DC1. Additional data are available in the JCB DataViewer at http://dx.doi.org/10.10831/jcb.201209077.dv.

We acknowledge Dr. Seth Alper for his comments and suggestions and E. Marino for technical support (National Institutes of Health U54-AI057159).

This work was supported by National Institutes of Health grants R01 GM075252 (T. Kirchhausen), R01 CA31798 (T.A. Springer), and R01 HL104006 (C.V. Carman).

Submitted: 13 September 2012
Accepted: 28 March 2013

References

Aird, W.C. 2007. Endothelium as a therapeutic target in sepsis. *Curr. Drug Targets*. 8:501–507. http://dx.doi.org/10.2174/138945007780362782

Antunes, F., and E. Cadenas. 2000. Estimation of H_2O_2 gradients across biomembranes. *FEBS Lett.* 475:121–126. http://dx.doi.org/10.1016/S0014-5793(00)01638-0

Bazzoni, G., and E. Dejana. 2004. Endothelial cell-to-cell junctions: molecular organization and role in vascular homeostasis. *Physiol. Rev.* 84:869–901. http://dx.doi.org/10.1152/physrev.00035.2003

Belousov, V.V., A.F. Fradkov, K.A. Lukyanov, D.B. Staroverov, K.S. Shakhbazov, A.V. Terskikh, and S. Lukyanov. 2006. Genetically encoded fluorescent indicator for intracellular hydrogen peroxide. *Nat. Methods*. 3:281–286. http://dx.doi.org/10.1038/nmeth866

Bement, W.M., H.Y. Yu, B.M. Burkel, E.M. Vaughan, and A.G. Clark. 2007. Rehabilitation and the single cell. *Curr. Opin. Cell Biol.* 19:95–100. http://dx.doi.org/10.1016/j.ceb.2006.12.001

Bretschneider, T., S. Diez, K. Anderson, J. Heuser, M. Clarke, A. Müller-Taubenberger, J. Köhler, and G. Gerisch. 2004. Dynamic actin patterns and Arp2/3 assembly at the substrate-attached surface of motile cells. *Curr. Biol.* 14:1–10. http://dx.doi.org/10.1016/j.cub.2003.12.005

Browning, E.A., S. Chatterjee, and A.B. Fisher. 2012. Stop the flow: a paradigm for cell signaling mediated by reactive oxygen species in the pulmonary endothelium. *Annu. Rev. Physiol.* 74:403–424. http://dx.doi.org/10.1146/annurev-physiol-020911-153324

Campbell, F.R. 1972. Ultrastructural studies of transmural migration of blood cells in the bone marrow of rats, mice and guinea pigs. *Am. J. Anat.* 135:521–535. http://dx.doi.org/10.1002/aja.1001350406

Carman, C.V. 2009a. Mechanisms for transcellular diapedesis: probing and pathfinding by 'invadosome-like protrusions'. *J. Cell Sci.* 122:3025–3035. http://dx.doi.org/10.1242/jcs.047522

Carman, C.V. 2009b. Transmigratory cups and invadosome-like protrusions: new aspects of diapedesis. *In* Leukocyte Adhesion: Current Topics in Membranes, Vol. 64. K. Ley, editor. Elsevier, Amsterdam. 297–333.

Carman, C.V., and T.A. Springer. 2004. A transmigratory cup in leukocyte diapedesis both through individual vascular endothelial cells and between them. *J. Cell Biol.* 167:377–388. http://dx.doi.org/10.1083/jcb.200404129

Carman, C.V., C.D. Jun, A. Salas, and T.A. Springer. 2003. Endothelial cells proactively form microvilli-like membrane projections upon intercellular adhesion molecule 1 engagement of leukocyte LFA-1. *J. Immunol.* 171:6135–6144.

Carman, C.V., P.T. Sage, T.E. Sciuto, M.A. de la Fuente, R.S. Geha, H.D. Ochs, H.F. Dvorak, A.M. Dvorak, and T.A. Springer. 2007. Transcellular diapedesis is initiated by invasive podosomes. *Immunity*. 26:784–797. http://dx.doi.org/10.1016/j.immuni.2007.04.015

Case, L.B., and C.M. Waterman. 2011. Adhesive F-actin waves: a novel integrin-mediated adhesion complex coupled to ventral actin polymerization. *PLoS ONE*. 6:e26631. http://dx.doi.org/10.1371/journal.pone.0026631

Chamberlain, J.K., and M.A. Lichtman. 1978. Marrow cell egress: specificity of the site of penetration into the sinus. *Blood*. 52:959–968.

Chhabra, E.S., and H.N. Higgs. 2007. The many faces of actin: matching assembly factors with cellular structures. *Nat. Cell Biol.* 9:1110–1121. http://dx.doi.org/10.1038/ncb1007-1110

Chicurel, M.E., C.S. Chen, and D.E. Ingber. 1998. Cellular control lies in the balance of forces. *Curr. Opin. Cell Biol.* 10:232–239. http://dx.doi.org/10.1016/S0955-0674(98)80145-2

Chin, A.C., and C.A. Parkos. 2007. Pathobiology of neutrophil transepithelial migration: implications in mediating epithelial injury. *Annu. Rev. Pathol.* 2:111–143. http://dx.doi.org/10.1146/annurev.pathol.2.010506.091944

Cho, Y., and P.P. De Bruyn. 1986. Internal structure of the postcapillary high-endothelial venules of rodent lymph nodes and Peyer's patches and the transendothelial lymphocyte passage. *Am. J. Anat.* 177:481–490. http://dx.doi.org/10.1002/aja.1001770406

Cinamon, G., V. Shinder, R. Shamri, and R. Alon. 2004. Chemoattractant signals and beta 2 integrin occupancy at apical endothelial contacts combine with shear stress signals to promote transendothelial neutrophil migration. *J. Immunol.* 173:7282–7291.

De Bruyn, P.P., S. Michelson, and T.B. Thomas. 1971. The migration of blood cells of the bone marrow through the sinusoidal wall. *J. Morphol.* 133:417–437. http://dx.doi.org/10.1002/jmor.1051330406

Drummond, G.R., S. Selemidis, K.K. Griendling, and C.G. Sobey. 2011. Combating oxidative stress in vascular disease: NADPH oxidases as therapeutic targets. *Nat. Rev. Drug Discov.* 10:453–471. http://dx.doi.org/10.1038/nrd3403

DuFort, C.C., M.J. Paszek, and V.M. Weaver. 2011. Balancing forces: architectural control of mechanotransduction. *Nat. Rev. Mol. Cell Biol.* 12:308–319. http://dx.doi.org/10.1038/nrm3112

Ehrlich, M., W. Boll, A. Van Oijen, R. Hariharan, K. Chandran, M.L. Nibert, and T. Kirchhausen. 2004. Endocytosis by random initiation and stabilization of clathrin-coated pits. *Cell*. 118:591–605. http://dx.doi.org/10.1016/j.cell.2004.08.017

Ehrlicher, A.J., F. Nakamura, J.H. Hartwig, D.A. Weitz, and T.P. Stossel. 2011. Mechanical strain in actin networks regulates FilGAP and integrin binding to filamin A. *Nature*. 478:260–263. http://dx.doi.org/10.1038/nature10430

Farooqui, R., and G. Fenteany. 2005. Multiple rows of cells behind an epithelial wound edge extend cryptic lamellipodia to collectively drive cell-sheet movement. *J. Cell Sci.* 118:51–63. http://dx.doi.org/10.1242/jcs.01577

Feng, D., J.A. Nagy, K. Pyne, H.F. Dvorak, and A.M. Dvorak. 1998. Neutrophils emigrate from venules by a transendothelial cell pathway in response to FMLP. *J. Exp. Med.* 187:903–915. http://dx.doi.org/10.1084/jem.187.6.903

Feng, D., J.A. Nagy, H.F. Dvorak, and A.M. Dvorak. 2002. Ultrastructural studies define soluble macromolecular, particulate, and cellular transendothelial cell pathways in venules, lymphatic vessels, and tumor-associated microvessels in man and animals. *Microsc. Res. Tech.* 57:289–326. http://dx.doi.org/10.1002/jemt.10087

Friedl, P., and D. Gilmour. 2009. Collective cell migration in morphogenesis, regeneration and cancer. *Nat. Rev. Mol. Cell Biol.* 10:445–457. http://dx.doi.org/10.1038/nrm2720

Galkin, V.E., A. Orlova, and E.H. Egelman. 2012. Actin filaments as tension sensors. *Curr. Biol.* 22:R96–R101. http://dx.doi.org/10.1016/j.cub.2011.12.010

Gauthier, N.C., M.A. Fardin, P. Roca-Cusachs, and M.P. Sheetz. 2011. Temporary increase in plasma membrane tension coordinates the activation of exocytosis and contraction during cell spreading. *Proc. Natl. Acad. Sci. USA*. 108:14467–14472. http://dx.doi.org/10.1073/pnas.1105845108

Gawlowski, D.M., J.N. Benoit, and H.J. Granger. 1993. Microvascular pressure and albumin extravasation after leukocyte activation in hamster cheek pouch. *Am. J. Physiol.* 264:H541–H546.

Geiger, B., J.P. Spatz, and A.D. Bershadsky. 2009. Environmental sensing through focal adhesions. *Nat. Rev. Mol. Cell Biol.* 10:21–33. http://dx.doi.org/10.1038/nrm2593

Gomez, G.A., R.W. McLachlan, and A.S. Yap. 2011. Productive tension: force-sensing and homeostasis of cell-cell junctions. *Trends Cell Biol.* 21:499–505. http://dx.doi.org/10.1016/j.tcb.2011.05.006

Griendling, K.K., D. Sorescu, and M. Ushio-Fukai. 2000. NAD(P)H oxidase: role in cardiovascular biology and disease. *Circ. Res.* 86:494–501. http://dx.doi.org/10.1161/01.RES.86.5.494

He, P. 2010. Leucocyte/endothelium interactions and microvessel permeability: coupled or uncoupled? *Cardiovasc. Res.* 87:281–290. http://dx.doi.org/10.1093/cvr/cvq140

Hoshi, O., and T. Ushiki. 1999. Scanning electron microscopic studies on the route of neutrophil extravasation in the mouse after exposure to the chemotactic peptide N-formyl-methionyl-leucyl-phenylalanine (fMLP). *Arch. Histol. Cytol.* 62:253–260. http://dx.doi.org/10.1679/aohc.62.253

Houk, A.R., A. Jilkine, C.O. Mejean, R. Boltyanskiy, E.R. Dufresne, S.B. Angenent, S.J. Altschuler, L.F. Wu, and O.D. Weiner. 2012. Membrane tension maintains cell polarity by confining signals to the leading edge during neutrophil migration. *Cell*. 148:175–188. http://dx.doi.org/10.1016/j.cell.2011.10.050

Hwa, C., A. Sebastian, and W.C. Aird. 2005. Endothelial biomedicine: its status as an interdisciplinary field, its progress as a basic science, and its translational bench-to-bedside gap. *Endothelium*. 12:139–151. http://dx.doi.org/10.1080/10623320500192016

Ikeda, S., M. Yamaoka-Tojo, L. Hilenski, N.A. Patrushev, G.M. Anwar, M.T. Quinn, and M. Ushio-Fukai. 2005. IQGAP1 regulates reactive oxygen species-dependent endothelial cell migration through interacting with Nox2. *Arterioscler. Thromb. Vasc. Biol.* 25:2295–2300. http://dx.doi.org/10.1161/01.ATV.0000187472.55437.af

Katsumi, A., J. Milanini, W.B. Kiosses, M.A. del Pozo, R. Kaunas, S. Chien, K.M. Hahn, and M.A. Schwartz. 2002. Effects of cell tension on the small GTPase Rac. *J. Cell Biol.* 158:153–164. http://dx.doi.org/10.1083/jcb.200201105

Kim, M.H., F.R. Curry, and S.I. Simon. 2009. Dynamics of neutrophil extravasation and vascular permeability are uncoupled during aseptic cutaneous wounding. *Am. J. Physiol. Cell Physiol.* 296:C848–C856. http://dx.doi.org/10.1152/ajpcell.00520.2008

Kolega, J. 1986. Effects of mechanical tension on protrusive activity and microfilament and intermediate filament organization in an epidermal epithelium moving in culture. *J. Cell Biol.* 102:1400–1411. http://dx.doi.org/10.1083/jcb.102.4.1400

Kumar, S., I.Z. Maxwell, A. Heisterkamp, T.R. Polte, T.P. Lele, M. Salanga, E. Mazur, and D.E. Ingber. 2006. Viscoelastic retraction of single living stress fibers and its impact on cell shape, cytoskeletal organization, and extracellular matrix mechanics. *Biophys. J.* 90:3762–3773. http://dx.doi.org/10.1529/biophysj.105.071506

Ley, K., C. Laudanna, M.I. Cybulsky, and S. Nourshargh. 2007. Getting to the site of inflammation: the leukocyte adhesion cascade updated. *Nat. Rev. Immunol.* 7:678–689. http://dx.doi.org/10.1038/nri2156

Lum, H., and K.A. Roebuck. 2001. Oxidant stress and endothelial cell dysfunction. *Am. J. Physiol. Cell Physiol.* 280:C719–C741.

Ma, X., H.E. Lynch, P.C. Scully, and M.S. Hutson. 2009. Probing embryonic tissue mechanics with laser hole drilling. *Phys. Biol.* 6:036004. http://dx.doi.org/10.1088/1478-3975/6/3/036004

Marchesi, V.T., and H.W. Florey. 1960. Electron micrographic observations on the emigration of leucocytes. *Q. J. Exp. Physiol. Cogn. Med. Sci.* 45:343–348.

Massol, R.H., W. Boll, A.M. Griffin, and T. Kirchhausen. 2006. A burst of auxilin recruitment determines the onset of clathrin-coated vesicle uncoating. *Proc. Natl. Acad. Sci. USA*. 103:10265–10270. http://dx.doi.org/10.1073/pnas.0603369103

McNeil, P.L., and S. Ito. 1990. Molecular traffic through plasma membrane disruptions of cells in vivo. *J. Cell Sci.* 96:549–556.

McNeil, P.L., and T. Kirchhausen. 2005. An emergency response team for membrane repair. *Nat. Rev. Mol. Cell Biol.* 6:499–505. http://dx.doi.org/10.1038/nrm1665

Millán, J., L. Hewlett, M. Glyn, D. Toomre, P. Clark, and A.J. Ridley. 2006. Lymphocyte transcellular migration occurs through recruitment of endothelial ICAM-1 to caveola- and F-actin-rich domains. *Nat. Cell Biol.* 8:113–123. http://dx.doi.org/10.1038/ncb1356

Moldovan, L., K. Mythreye, P.J. Goldschmidt-Clermont, and L.L. Satterwhite. 2006. Reactive oxygen species in vascular endothelial cell motility. Roles of NAD(P)H oxidase and Rac1. *Cardiovasc. Res.* 71:236–246. http://dx.doi.org/10.1016/j.cardiores.2006.05.003

Murrell, M., R. Kamm, and P. Matsudaira. 2011. Tension, free space, and cell damage in a microfluidic wound healing assay. *PLoS ONE.* 6:e24283. http://dx.doi.org/10.1371/journal.pone.0024283

Orr, A.W., B.P. Helmke, B.R. Blackman, and M.A. Schwartz. 2006. Mechanisms of mechanotransduction. *Dev. Cell.* 10:11–20. http://dx.doi.org/10.1016/j.devcel.2005.12.006

Paluch, E., J. van der Gucht, and C. Sykes. 2006. Cracking up: symmetry breaking in cellular systems. *J. Cell Biol.* 175:687–692. http://dx.doi.org/10.1083/jcb.200607159

Radice, G.P. 1980. The spreading of epithelial cells during wound closure in *Xenopus* larvae. *Dev. Biol.* 76:26–46. http://dx.doi.org/10.1016/0012-1606(80)90360-7

Rajfur, Z., P. Roy, C. Otey, L. Romer, and K. Jacobson. 2002. Dissecting the link between stress fibres and focal adhesions by CALI with EGFP fusion proteins. *Nat. Cell Biol.* 4:286–293. http://dx.doi.org/10.1038/ncb772

Raucher, D., and M.P. Sheetz. 2000. Cell spreading and lamellipodial extension rate is regulated by membrane tension. *J. Cell Biol.* 148:127–136. http://dx.doi.org/10.1083/jcb.148.1.127

Rodrigues, S.F., and D.N. Granger. 2010. Role of blood cells in ischaemia-reperfusion induced endothelial barrier failure. *Cardiovasc. Res.* 87:291–299. http://dx.doi.org/10.1093/cvr/cvq090

Sage, P.T., and C.V. Carman. 2009. Settings and mechanisms for trans-cellular diapedesis. *Front. Biosci.* 14:5066–5083. http://dx.doi.org/10.2741/3587

Sage, P.T., L.M. Varghese, R. Martinelli, T.E. Sciuto, M. Kamei, A.M. Dvorak, T.A. Springer, A.H. Sharpe, and C.V. Carman. 2012. Antigen recognition is facilitated by invadosome-like protrusions formed by memory/effector T cells. *J. Immunol.* 188:3686–3699. http://dx.doi.org/10.4049/jimmunol.1102594

Shaw, S.K., P.S. Bamba, B.N. Perkins, and F.W. Luscinskas. 2001. Real-time imaging of vascular endothelial-cadherin during leukocyte transmigration across endothelium. *J. Immunol.* 167:2323–2330.

Shifrin, Y., P.D. Arora, Y. Ohta, D.A. Calderwood, and C.A. McCulloch. 2009. The role of FilGAP-filamin A interactions in mechanoprotection. *Mol. Biol. Cell*. 20:1269–1279. http://dx.doi.org/10.1091/mbc.E08-08-0872

Sinha, B., D. Köster, R. Ruez, P. Gonnord, M. Bastiani, D. Abankwa, R.V. Stan, G. Butler-Browne, B. Vedie, L. Johannes, et al. 2011. Cells respond to mechanical stress by rapid disassembly of caveolae. *Cell*. 144:402–413. http://dx.doi.org/10.1016/j.cell.2010.12.031

Tambe, D.T., C.C. Hardin, T.E. Angelini, K. Rajendran, C.Y. Park, X. Serra-Picamal, E.H. Zhou, M.H. Zaman, J.P. Butler, D.A. Weitz, et al. 2011. Collective cell guidance by cooperative intercellular forces. *Nat. Mater.* 10:469–475. http://dx.doi.org/10.1038/nmat3025

Taulet, N., V.D. Delorme-Walker, and C. DerMardirossian. 2012. Reactive oxygen species regulate protrusion efficiency by controlling actin dynamics. *PLoS ONE*. 7:e41342. http://dx.doi.org/10.1371/journal.pone.0041342

Terada, L.S. 2006. Specificity in reactive oxidant signaling: think globally, act locally. *J. Cell Biol.* 174:615–623. http://dx.doi.org/10.1083/jcb.200605036

Thureson-Klein, A., P. Hedqvist, and L. Lindbom. 1986. Leukocyte diapedesis and plasma extravasation after leukotriene B4: lack of structural injury to the endothelium. *Tissue Cell*. 18:1–12. http://dx.doi.org/10.1016/0040-8166(86)90002-9

Touyz, R.M., G. Yao, M.T. Quinn, P.J. Pagano, and E.L. Schiffrin. 2005. p47phox associates with the cytoskeleton through cortactin in human vascular smooth muscle cells: role in NAD(P)H oxidase regulation by angiotensin II. *Arterioscler. Thromb. Vasc. Biol.* 25:512–518. http://dx.doi.org/10.1161/01.ATV.0000154141.66879.98

Ushio-Fukai, M. 2006. Localizing NADPH oxidase-derived ROS. *Sci. STKE*. 2006:re8. http://dx.doi.org/10.1126/stke.3492006re8

Vicker, M.G. 2002. F-actin assembly in *Dictyostelium* cell locomotion and shape oscillations propagates as a self-organized reaction-diffusion wave. *FEBS Lett.* 510:5–9. http://dx.doi.org/10.1016/S0014-5793(01)03207-0

Vogel, V., and M. Sheetz. 2006. Local force and geometry sensing regulate cell functions. *Nat. Rev. Mol. Cell Biol.* 7:265–275. http://dx.doi.org/10.1038/nrm1890

Weiner, O.D., W.A. Marganski, L.F. Wu, S.J. Altschuler, and M.W. Kirschner. 2007. An actin-based wave generator organizes cell motility. *PLoS Biol.* 5:e221. http://dx.doi.org/10.1371/journal.pbio.0050221

Wojciak-Stothard, B., and A.J. Ridley. 2002. Rho GTPases and the regulation of endothelial permeability. *Vascul. Pharmacol.* 39:187–199. http://dx.doi.org/10.1016/S1537-1891(03)00008-9

Woodfin, A., M.B. Voisin, M. Beyrau, B. Colom, D. Caille, F.M. Diapouli, G.B. Nash, T. Chavakis, S.M. Albelda, G.E. Rainger, et al. 2011. The junctional adhesion molecule JAM-C regulates polarized transendothelial migration of neutrophils in vivo. *Nat. Immunol.* 12:761–769. http://dx.doi.org/10.1038/ni.2062

Yang, L., R.M. Froio, T.E. Sciuto, A.M. Dvorak, R. Alon, and F.W. Luscinskas. 2005. ICAM-1 regulates neutrophil adhesion and transcellular migration of TNF-alpha-activated vascular endothelium under flow. *Blood*. 106:584–592. http://dx.doi.org/10.1182/blood-2004-12-4942

Yu, Q.C., and P.L. McNeil. 1992. Transient disruptions of aortic endothelial cell plasma membranes. *Am. J. Pathol.* 141:1349–1360.

Published April 29, 2013

Martinelli et al., http://www.jcb.org/cgi/content/full/jcb.201209077/DC1

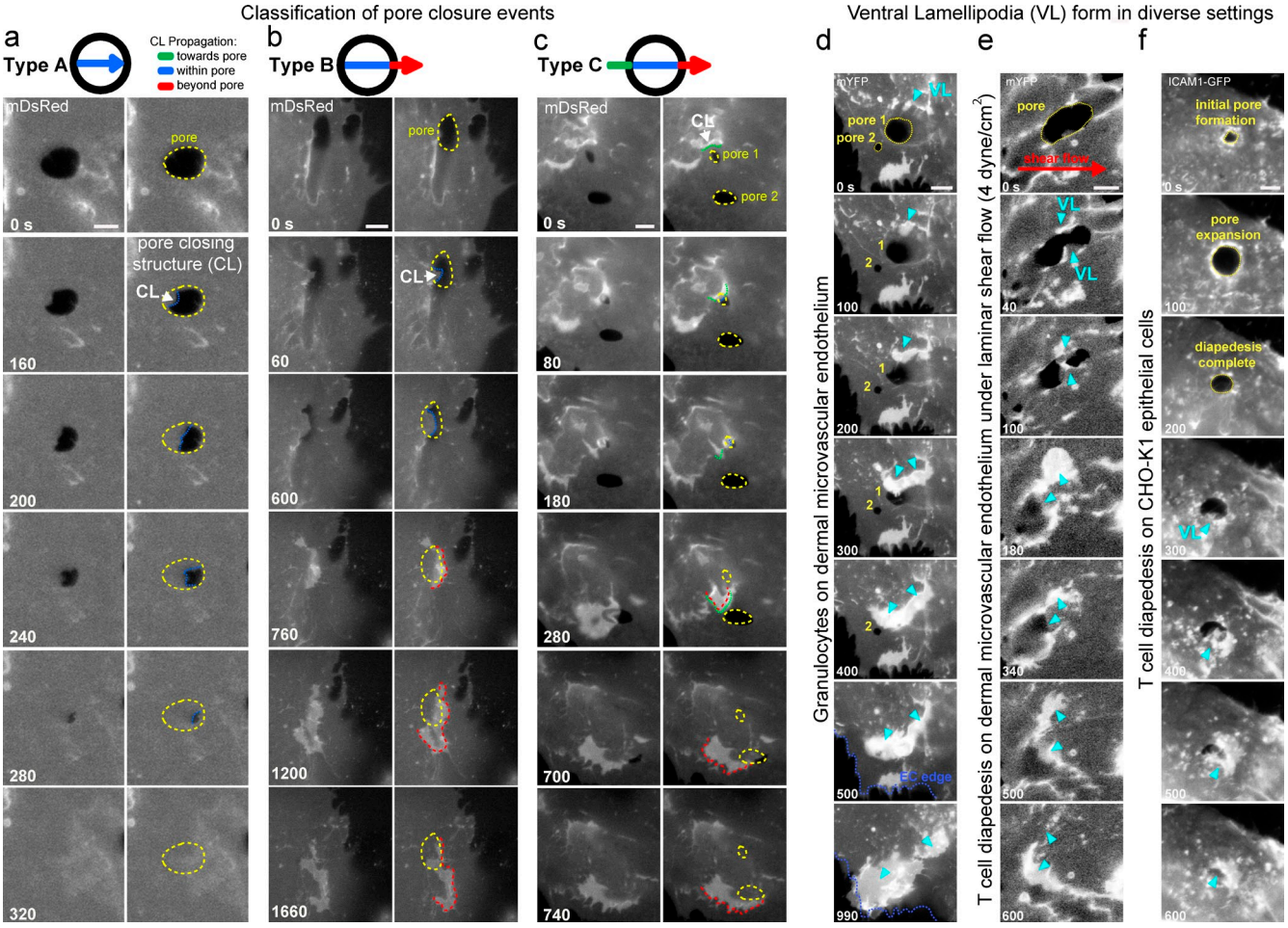

Figure S1. **Classification of pore closure events in diverse settings.** Classification of pore closure events. Live-cell imaging of pore closure after lymphocyte diapedesis across MVECs expressing mDsRed. Yellow dashed lines indicate the open pore in the endothelium. Dashed blue lines indicate propagation of closing protrusions within the pore. Green and red lines, respectively, represent phases of protrusion propagation outside of the pore moving toward it before closure or away from it afterward. (a) A representative type A closure. Propagation occurs within the confines of the pore only, moving from one edge to the opposite one. (b) A representative type B closure. Protrusion initiates at a pore edge and continues to propagate beyond the distal edge of the pore after closing it. Note that in the selected example the protrusion is initiated well before the T cell has completely exited the pore. (c) A representative type C closure. Protrusion initiates distant from the pore and migrates toward, across, and beyond it. Note that the selected event is also an example of successive propagation across and closure of two adjacent pores (pore 1 and 2). See also Video 2, Part I. Closure proceeds similarly through VL in diverse settings. (d) Live-cell imaging during granulocyte transcellular diapedesis across mYFP-expressing MVECs. Note that the VL (arrowheads) initiates distant from one pore, travels across (and closes) two distinct pores (1 and 2) in succession, and continues to extend beyond the edge of the cell (dashed blue line) to close a paracellular gap (type C closure). (e) Diapedesis as in A, performed with T cells under physiological laminar fluid shear flow (4 dyne/cm^2; red arrow). Note that two distinct VL form on opposite sides of the pore to close it and continue propagation briefly (type B closure). (f) Transcellular diapedesis of T cells across CHO-K1 epithelial cells expressing ICAM-1-GFP. Note VL initiates slightly outside of, and continues to propagate beyond, the pore (type C closure). Arrowheads indicate pore-closing VL. See also Video 2, Part II. Bars, 5 µm.

Published April 29, 2013

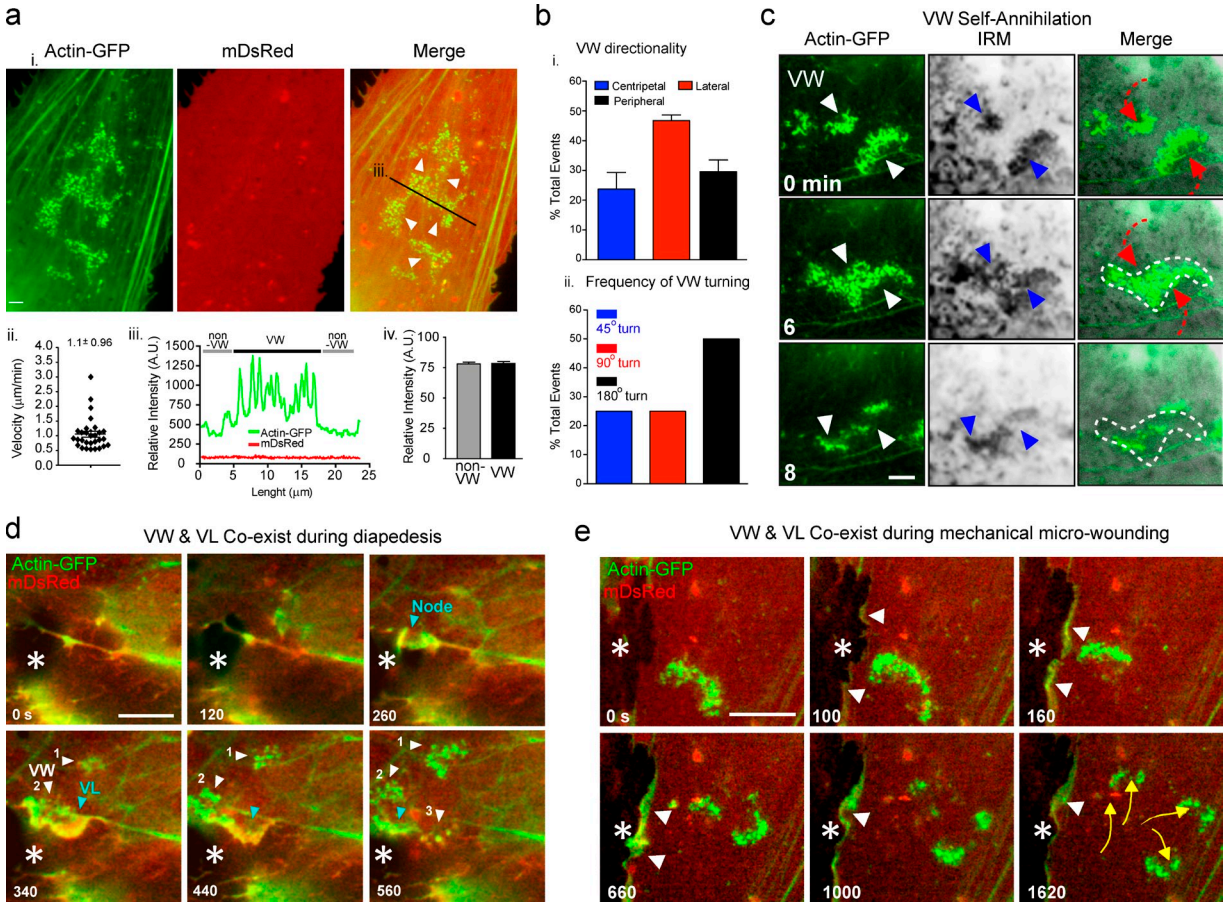

Figure S2. **VL coexist with VW in endothelial cells.** (a) MVECs transfected with mDsRed and actin-GFP were imaged live in the absence of leukocytes, TNF pretreatment, or any other stimulus. Representative images (from >30 separate samples) show spontaneously formed actin waves (WV) characterized by actin punctae (i) that traveled ~1 μm/min (ii) without membrane protrusion (iii). (i) Fluorescence intensity line scan from right panel shows that peaks in the actin signal (green line), which correspond to individual actin punctae of a wave, are not coupled to changes in the membrane intensity (red line). (iv) Quantification of membrane fluorescence intensity in non-VW and VW ROIs. Values represent means ± SEM (n > 10). (b) Quantitative analysis of VW propagation directionality with respect to endothelial cell axes of symmetry (i). Values represent means ± SEM (n = 3). (ii.) The frequency of ~45°, ~90°, and ~180° turns during VW propagation was determined from analysis of >50 micro-wound closure events. (c) Combined fluorescence microscopy (left) and IRM (middle, arrowheads) of MVECs transfected with actin-GFP and mDsRed (not depicted) shows that these waves protrude ventrally against the substrate and exhibit swirling propagation (red arrowheads and dashed line) and self-annihilation upon intersection (white dotted line). (d) Imaging of actin dynamics during closure of a lymphocyte diapedesis pore (asterisks) showing that VL initiate from nodes of actin accumulated on preformed fibers (cyan arrowheads). Additionally, VW (white arrowheads) propagate independently from (1) and coordinately with (2 and 3) VL during pore closing events. See also Video 4, Part I, ex. 3. (e) Imaging of actin dynamics during mechanical micro-wound closure shows coexistence of wound-responsive VL (white arrowheads) and nonresponsive VW (yellow arrows). Asterisk indicates site of mechanical probe wounding of a neighbor cell.

Published April 29, 2013

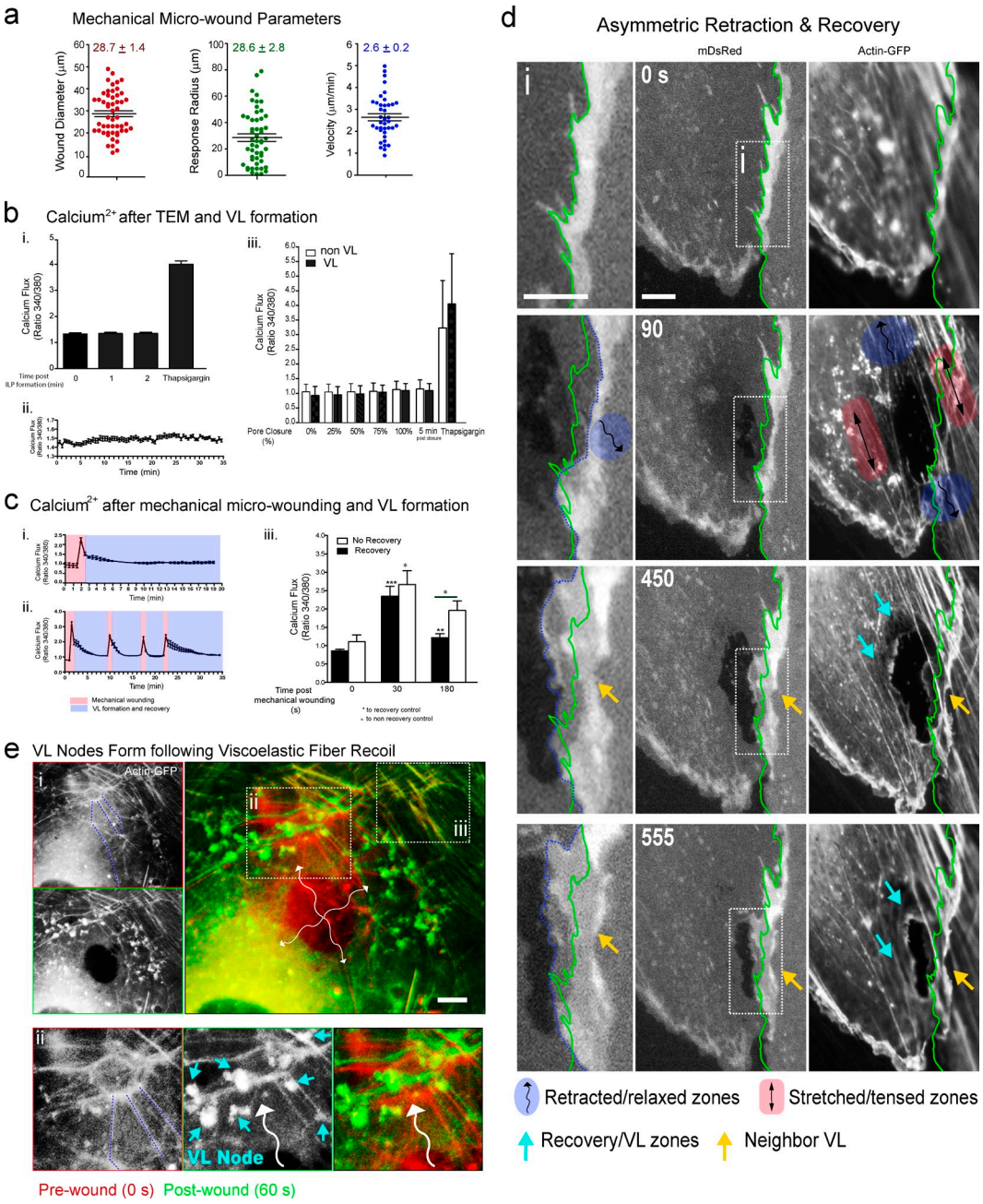

Figure S3. **Mechanical micro-wounding and response to tension breakage.** (a) Quantitative analysis of mechanical micro-wounding and response parameters. (b) Calcium responses during leukocyte diapedesis and mechanical micro-wounding pore closure. MVECs transfected with mDsRed and actin-GFP were loaded with Fura-2AM and then imaged during leukocyte diapedesis (b) or mechanical micro-wounding (c). (b, i) Calcium responses (measured as ratio 340:380) in the imaging frame immediately before (0), in the two frames (1 and 2, taken at 20 s intervals) after initial leukocyte-mediated transcellular pore formation, or in the frame immediately after addition of thapsigargin (positive control). $n = 3$. (ii) Calcium flux recorded continuously during persistent leukocyte diapedesis over a 35-min duration. $n = 3$. (iii) Calcium ratios were calculated at different stages of pore closure (i.e., percentage of completion) for VL and non-VL areas. $n = 8$. (c) Calcium responses were recording during single (i) and multiple sequential (ii) mechanical micro-wounding events. Blue regions represent the time frames corresponding to the initiation of VL and onset of pore closure. Failure to close pores correlated with failure to normalize calcium. Calcium ratios at 30 and 180 s after mechanical micro-wounding are shown. (iii) Non-closing pores failed to normalize calcium significantly below a ratio of 2. Values represent means ± SEM ($n > 3$). Statistical significance is indicated with p-values as follows: ***, $P < 0.001$; **, $P < 0.01$; *, $P < 0.05$. (d) Asymmetric retraction and recovery of mechanical micro-wounds. Wounding in a region of parallel actin stress fibers results in asymmetric viscoelastic recoil/relaxation in discrete regions (shaded blue) in antiparallel directions. Adjacent untouched fibers undergo visible extension, presumably because of compensatory force loading (red shaded areas). Robust VL and VW recovery responses predominantly formed in the relaxed (cyan arrows) but not the stretched areas (red shading). Dashed green and blue lines, respectively, indicate the original and current position of the intercellular junction adjacent to the transcellular micro-wound. At 90 s after wounding, a substantial degree of retraction of the intact junction toward the untouched neighbor is evident. Strong localized VL responses were seen from the neighbor precisely at the site of the initial relaxation (yellow arrow), formed within 80 s of micro-wounding (not depicted) and sustained at 450 and 555 s later. See also corresponding Video 6 and compare/contrast with Fig. 7 a. (e) Zones of viscoelastic recoil in actin networks form nodes of VL initiation on intact fibers. Images of actin-GFP immediately before and after micro-wounding were differentially pseudo-colored and overlaid. This representation highlights the displacement of intact actin networks at sites distant from, but originally tethered to, fibers that were broken during wounding. These highly displaced fibers become preferential loci for accumulation of actin nodes and VL (cyan arrows). See Video 7, ex. 2. Bars, 5 µm.

Published April 29, 2013

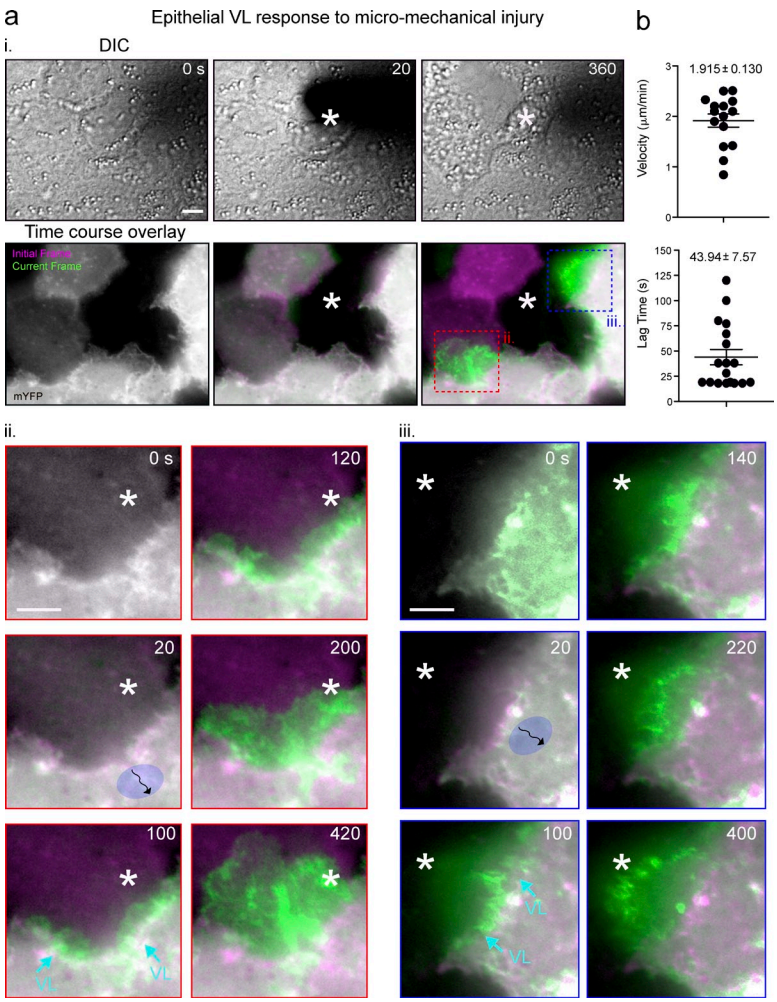

Figure S4. **Epithelial VL response after mechanical micro-wounding.** MDCK cells transfected with mDsRed and actin-GFP were imaged live during mechanical micro-wound recovery. (a, i, top) DIC images of a confluent monolayer being probe wounded (dark area, asterisk). (bottom) Actin-GFP fluorescence (of the positive transfectants within the monolayer) with the initial (magenta) and subsequent (green) time points overlayed. (ii and iii) Zoomed regions showing additional time points of boxed areas in i. Note that immediately after wounding a narrow magenta region is evident at the edges of the cell facing the wound, indicating cell retraction. In subsequent frames strong green signal of VL (cyan arrows) spreading toward the wound are evident. (b) Quantification of epithelial VL propagation velocity and lag time until formation of first VL after micro-wound. Values represent means ± SEM ($n > 30$). Bars, 5 μm.

Published April 29, 2013

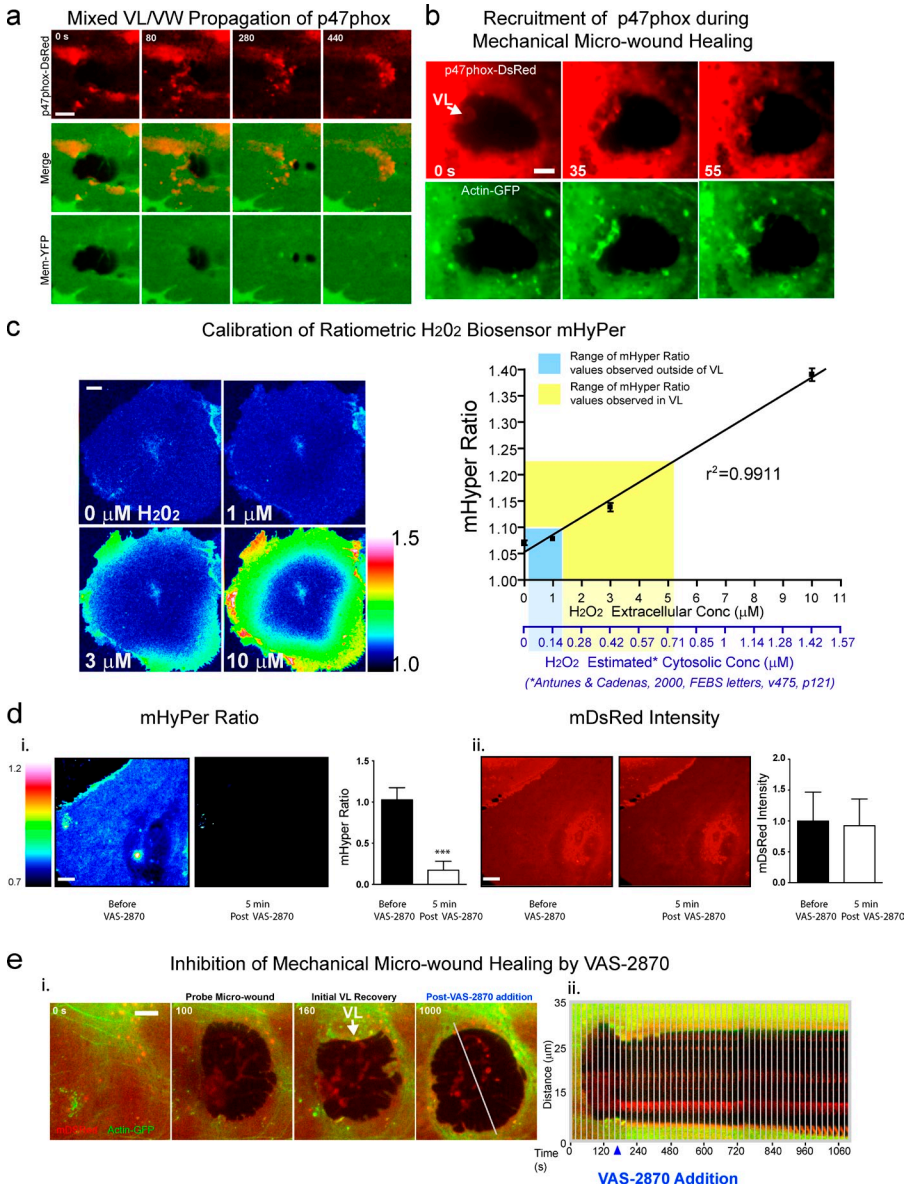

Figure S5. **Characterizing p47phox and H_2O_2 production in micro-wound healing.** (a) Closure of a transcellular pore in MVECs coexpressing mYFP and p47phox-DsRed. Note enrichment of p47phox both in the VL leading edge (see 80 s) and in VW type punctae that continue to propagate after pore closure (280 and 440 s). (b) Representative closure of a mechanical micro-wound in MVEC coexpressing actin-GFP and p47phox-DsRed. White arrow indicates an actin-rich VL with colocalized enrichment of p47phox. (c) MVECs expressing mHyPer were subjected to ratiometric imaging upon addition of the indicated concentrations of exogenous H_2O_2 (left). Mean ratios were calculated for each concentration and plotted against the corresponding concentration of H_2O_2 and subjected to linear regression (right). The estimated intracellular concentration of H_2O_2 is known to be approximately one seventh of that which is added exogenously (Antunes and Cadenas, 2000). Based on this, an estimated intracellular H_2O_2 x-axis scale is shown. Colorimetric range indicators show the observed VL (yellow) and non-VL (blue) mHyPer ratios and the corresponding estimation of intracellular H_2O_2 concentrations that they reflect. (d) MVECs coexpressing mHyPer and mDsRed were imaged before and 5 min after addition of 15 μM VAS-2870. Representative images and quantitation of mHyper ratios (i) and mDsRed intensity (ii) are shown (n = 3). Statistical significance is indicated with p-value: ***, $P < 0.001$. Error bars represent SEM. (e) Representative blockade of VL and wound healing after probe-induced micro-wounding of MVEC coexpressing mDsRed and actin-GFP. Selected frames show MVEC immediately before and after micro-wounding, after initiation of VL, and after addition of the NADPH oxidase inhibitor VAS-2870 (left). White line shows position used to generate a kymograph (right). Note that VL immediately retract and wound fails to close after addition of VAS-2870. Bars, 5 μm.

Published April 29, 2013

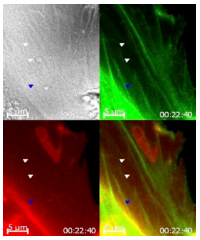

Video 1. **Leukocyte-driven endothelial micro-wounds are closed efficiently.** (Part I) Directed lamellipodia heal leukocyte-mediated vascular micro-wounds. Live-cell imaging of lymphocyte diapedesis on MVECs transfected with actin-GFP (green) and mDsRed (red), corresponding to Fig. 1 b. Boxed regions A and B are expanded in bottom panels. (A) A burst of lamellar activity that rapidly closes a transcellular migration pore immediately after completion of diapedesis, which continues to travel a significant distance beyond the pore. Boxed region B and asterisk in top panel show related processes during closure of paracellular diapedesis gaps (see Fig. 3 for further explanation). (Part II) Membrane doubling/folding is associated with closing lamellipodia. Live-cell imaging of lymphocyte transcellular diapedesis across MVECs transfected with actin-GFP (green) and mDsRed (red) corresponding to Fig. 1 e. Arrowheads indicate initiation of actin protrusions at the edge of the pore (white) and adjacent to it (blue), which seem to emerge from preformed fibers, as the leukocyte completes diapedesis. These expand quickly and propagated across the pore to the MVEC cell periphery in coordination with lymphocyte movement between the cell and the substratum. The clearly evident doubling of the fluorescence membrane signal around these structures demonstrates that membrane is folded around them and that they are propagating as frank membrane protrusions. Images were acquired by time-lapse microscopy using a microscope (Axiovert 200M; Carl Zeiss). Frames were taken every 30 s for 26 min (Part I) or 20 s for 22 min and 40 s (Part II).

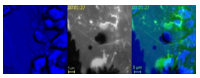

Video 2. **Classification of closing lamellipodia in diverse settings.** (Part I) Live-cell imaging of pore closure after lymphocyte diapedesis across MVECs expressing mYFP, corresponding to Fig. S1 (a–c). Representative examples of type A, B, and C pore closures are shown sequentially. (Part II) Live-cell imaging of transmigration in three distinct settings corresponding to Fig. S1 (d–f). Example 1 shows a granulocytes migrating across a MVEC expressing mYFP and successive closure of two distinct pores by a single VL. Example 2 shows transcellular migration of a T cell under 4 dyne/cm^2 laminar fluid shear flow and closure of a single pore by two distinct VL traveling in opposite directions. Example 3 shows transcellular diapedesis of a lymphocyte across an ICAM-1-GFP–expressing CHO-K1 epithelial cell, which is closed by a VL-mediated process not unlike those seen in MVECs. Images were acquired by time-lapse microscopy using a microscope (Axiovert 200M; Carl Zeiss). Frames were taken every 25 s for 4 min and 45 s (type A), 20 s for 28 min and 40 s (type B), 20 s for 14 min and 40 s (type C), 25 s for 10 min (Part II, ex. 1), 25 s for 26 min and 5 s (Part II, ex. 2), or 22 s for 28 min and 8 s (Part II, ex. 3).

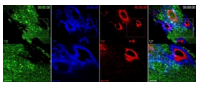

Video 3. **VL heal endothelial micro-wounds.** Live-cell serial-section spinning disk confocal imaging of lymphocytes migrating on MVECs expressing m-YFP, corresponding to Fig. 2 b. Time-lapse video shows select basal/ventral (green), intermediate (blue), and apical/dorsal (red) confocal sections both separately and overlaid. A wide-field view showing five separate transmigration pore closure events (as well as several gap closures) and a zoomed in view of three of them is shown sequentially. Note that lamellar structures are clearly, and exclusively, ventral (i.e., green) spread out under the pores (initially visibly open in the intermediate and dorsal section), effectively closing them from the bottom. Images were acquired by time-lapse microscopy using a spinning disk confocal microscope (Axiovert 200M; Carl Zeiss). Frames were taken every 20 s for 6 min and 40 s.

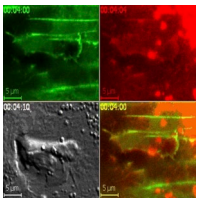

Video 4. **Complex features of VL initiation and propagation.** (Part I) VL form at site of preexisting actin filaments. Live-cell imaging of lymphocyte migration on MVECs transfected with actin-GFP (green) and mDsRed (red), corresponding to Fig. 4. In three sequential examples, extensive and complex micro-distortions of membrane and actin cytoskeleton are generated in MVECs by T cells as they form migration pores and spread under the endothelium (disrupting MVEC–substrate adhesion in the process). In all cases, preformed actin filaments in the distortion zone serve as predominant VL nucleation sites whereby a node or quasi-orthogonal spike appears briefly (~20–40 s) and then abruptly transitions to a VL. Additionally, some evidence for both independent and coordinated VL and VW propagation can be seen in example 3 (see Fig. S2 d and legend for details). (Part II) Directional propagation features of VL. Live-cell imaging of lymphocyte migration on MVECs transfected with mDsRed (red; and, in ex. 3, actin-GFP [green] as well) corresponding to Fig. 5. Example 1 shows closure of a single pore by two distinct VL traveling in opposite directions (corresponding to Fig. 5 b). Example 2 shows sequential closure of a transcellular pore and a paracellular gap by a single VL. This VL initially turns nearly 180° to close the pore and subsequently adjusts ~90° in the opposite direction to steer toward and close the gap (corresponding to Fig. 5 d). Example 3 shows a larger field of view in which multiple diapedesis pores and gaps are formed in mDsRed (red)- and actin-GFP (green)–expressing MVECs (corresponding to Fig. 5 f). This video provides a representative of the ability of the endothelium to coordinate complex propagation of multiple VL to close concomitantly formed discontinuities. Also note the apparent mixed VL and VW propagation, whereby VW seem to persist after micro-wound closure and VL extinction. Images were acquired by time-lapse microscopy using a microscope (Axiovert 200M; Carl Zeiss). Frames were taken every 20 s for 13 min and 40 s (Part I, ex. 1), 20 s for 11 min and 20 s (Part I, ex. 2), 22 s for 24 min and 22 s (Part I, ex. 3), 20 s for 14 min and 20 s (Part II, ex. 1), 20 s for 27 min and 30 s (Part II, ex. 2), or 20 s for 15 min and 10 s (Part II, ex. 3).

Published April 29, 2013

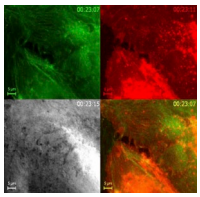

Video 5. **Closure events after mechanical micro-wounding.** (Part I) Sequential transcellular micromechanical wounding and healing events in a single MVEC. Live-cell imaging of transcellular mechanical micro-wounding in an MVEC transfected with actin-GFP (green) and mDsRed (red), corresponding to Fig. 6 b. A single MVEC was subjected to four sequential mechanical micro-wounding events (see numbers in bottom right panel). Each time the initial wound rapidly expands as broken adhesions and cytoskeleton caused viscoelastic recoil of preexisting tension. The MVEC then rapidly formed nodes of actin in a large ∼20–30-µm radius around the pore with mixed VL and VW features. These exhibit directed propagation into the micro-wound to close it. The ventral nature of these structures can clearly be seen by dark regions in IRM (bottom left). Bars, 5 µm. (Part II) Closure event after paracellular mechanical micro-wounding. Live-cell imaging of paracellular mechanical micro-wound in MVEC transfected with actin-GFP (green) and mDsRed (red). By placing the probe tip over one cell near its junction a paracellular gap is formed. Significant viscoelastic recoil is evident in both the wounded cell and the untouched neighbor (particularly evident in the bottom right corner) that correlates with a highly robust VL and VW recovery response. The ventral nature of these structures can be seen by the appearance of dark spots in IRM (bottom left). Bars, 5 µm. Images were acquired by time-lapse microscopy using a microscope (Axiovert 200M; Carl Zeiss). Frames were taken every 20 s for 45 min (Part I) or 20 s for 28 min and 20 s (Part II).

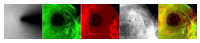

Video 6. **Asymmetric retraction and recovery after mechanical micro-wounding.** Live-cell imaging of transcellular mechanical wounding in MVECs coexpressing actin-GFP (green) and mDsRed (red), corresponding to Fig. 7 a and Fig. S3 d. Whereas the first example shows both predominant retraction and subsequent VL/VW recovery in orthogonally oriented directions (i.e., toward the top and bottom left corners), in the second example retraction and recovery both predominantly occur in antiparallel directions (i.e., toward the top left and bottom right corners). In both cases the nonresponding regions opposite the major recoil/response areas are visibly stretched and, therefore, tensed during wounding. In both examples the broken isometric tension is visibly transmitted to discrete regions of the unwounded neighbor cells through intact adherens junctions that retract and translate toward the neighboring cell (right side). In response, the untouched cells produce an avid VL response precisely in the location where retraction occurred. The ventral nature of these response structures is shown by the appearance of dark spots in IRM (fourth panel). Bars, 5 µm. Images were acquired by time-lapse microscopy using a microscope (Axiovert 200M; Carl Zeiss). Frames were taken every 20 s for 19 min and 20 s (ex. 1) or 20 s for 14 min and 40 s (ex. 2).

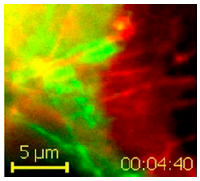

Video 7. **Tension release correlates with VL initiation on actin filaments.** Live-cell imaging of mechanical wounding in MVECs coexpressing actin-GFP and mDsRed (not depicted), corresponding to Figs. 7 b and S3 e. MVECs were mechanically wounded paracellularly (ex. 1) or transcellulary (ex. 2). To better understand the relationship between the viscoelastic recoil that develops rapidly in the cytoskeleton after wounding, and the subsequent formation of actin nodes and VL, we froze the prewound actin image into the left panel and the red channel of the right panel and placed the full dynamic time-lapse series in the middle panels and green channel of the right panel. In the color overlaid panel on the right, the first frame has time-matched green and red images that show perfect colocalization yielding a yellow image. After micro-wound the progressive time series images in green become separated from the original alignment for an intuitive visualization of recoil response. Areas that undergo the most significant retraction exhibit predominant formation of nodes and VL (which were confirmed as such via IRM and membrane signal (acquired but not depicted). Images were acquired by time-lapse microscopy using a microscope (Axiovert 200M; Carl Zeiss). Frames were taken every 20 s for 9 min (ex. 1) or 15 s for 6 min (ex. 2).

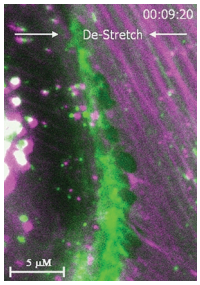

Video 8. **Enforced substrate compression initiates putative VL.** Live-cell imaging of a confluent MVEC monolayer coexpressing actin-GFP and mYFP during an acute 10% uniaxial compression/de-stretch of the substrate, corresponding to Fig. 8 b (ii). To better visualize the initial de-stretch and the subsequent VL formation, we froze the first frame (magenta) and superimposed the time-lapsed images (green). Putative VL activity can be seen emanating from the ends of actin filaments that are partially aligned with the axis of de-stretch. For individual filaments, note the similarity to Video 1 B, showing paracellular gap closure after diapedesis micro-wounding. Shown is one representative experiment of at least 10 independent experiments. Images were acquired by time-lapse microscopy using a microscope (Axiovert 200M; Carl Zeiss). Frames were taken every 35 s for 11 min and 45 s

Published April 29, 2013

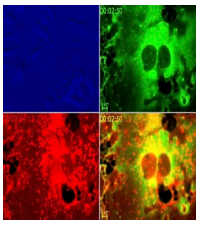

Video 9. **Role of Rho-GTPases on pore closure.** (Part I) Effect of Rac1 inhibitor NSC23766 on pore closure. Representative live-cell imaging of reversible VL inhibition during diapedesis on MVECs expressing mYFP that is analogous to Fig. 9 c. In initial frames, six diapedesis events can be seen in progress. At 5 min, as indicated, the Rac1 inhibitor NSC23677 (500 µM) was added. Over the next ~18 min all of the original pores and gaps, as well as some additionally formed micro-wounds, are present, despite completion of most of the diapedesis events. After drug washout the accumulated micro-wounds were rapidly closed by a concerted mobilization of multiple independent and steered VL. (Part II) Effect of Rho kinase inhibitor Y27632 on micro-wound healing. Live-cell imaging of T cell diapedesis on MVECs coexpressing mDsRed (red) and actin-GFP (green) during addition of the Rho kinase inhibitor Y27632. During the initial 5 min, in the setting of high lymphocyte density, multiple diapedesis events are seen at various stages and some VL have formed to initiate pore closure. During addition of Y27632 (90 µM), robust steered VL closure activity proceeds uninterrupted for >25 min, progressively closing each micro-wound as individual diapedesis events reach completion. Separate studies in the absence of leukocytes confirm that drug is active at this concentration at reducing stress fiber density within minutes of addition (not depicted). Bars, 5 µm. Images were acquired by time-lapse microscopy using a microscope (Axiovert 200M; Carl Zeiss). Frames were taken every 20 s for 50 min and 50 s (Part I) or 20 s for 31 min and 50 s (Part II).

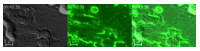

Video 10. **ROS play a role in VL propagation.** (Part I) The NADPH oxidase subunit p47phox is enriched in VL. Representative live-cell imaging of p47phox distribution dynamics during diapedesis. MVECs were cotransfected with p47phox-DsRed (red) and either mYFP (green; ex. 1) or actin-GFP (green; ex. 2, corresponding to Fig. 10 a). Example 1 shows leading edge enrichment of p47phox in VL during closure of a paracellular gap. Example 2 shows p47phox coenriched with actin at nodes of VL initiation and in VL leading edge, which propagate successively across a transcellular pore and then a paracellular gap. IRM shown on the far right indicates VL initiate and propagate in close apposition to the substrate. (Part II) Effect of ROS inhibitors on VL-mediated pore closure. Representative live-cell imaging of reversible blockade of VL by ROS inhibitors during diapedesis corresponding to Fig. 10 d. MVECs expressing mYFP were imaged during lymphocyte diapedesis. Where indicated, inhibitors of NAPDH oxidase signaling apocynin (1 mM; ex. 1) or Tempol (500 µM; ex. 2) were added and then at later times washed out (as indicated). In both cases micro-wounds remained patent during the 15-min incubation with drug, and washout led to immediate mobilization of steered VL and micro-wound healing. Images were acquired by time-lapse microscopy using a microscope (Axiovert 200M; Carl Zeiss). Frames were taken every 25 s for 29 min and 5 s (Part I, ex. 1), 20 s for 12 min and 5 s (Part I, ex. 2), 45 s for 46 min and 45 s (Part II, ex. 1), or 45 s for 42 min and 25 s (Part II, ex. 2).

Reference

Antunes, F., and E. Cadenas. 2000. Estimation of H_2O_2 gradients across biomembranes. *FEBS Lett.* 475:121–126. http://dx.doi.org/10.1016/S0014-5793(00)01638-0